Study of novel properties of graphene-ZnO hetrojunction interface using density functional theory

Hailu Diro

A Thesis submitted to
The Department of Physics

Presented in Partial fulfilment of the Requirements for the
Degree of Master of Science (Physics)

Addis Ababa University
Addis Ababa, Ethiopia
March 2023

Addis Ababa University
College of Natural Sciences
School of Graduate Studies

This is to certify that the thesis prepared by Hailu Diro entitled: *Study of novel properties of Graphene-ZnO interface using density functional theory* and submitted for partial fulfillment of the requirements for the Degree of Master of Science complies with the regulations of the University and meets the accepted standards with respect to originality and quality.

Signed by the Examining Committee:

Examiners

1. Dr. Lemi Demeyu Signature .... Date ....

2. Dr. Yitageu Elfagd Signature .... Date ....

Advisor(s)

1. Dr. Kenate Nemera Signature .... Date ....

Chair of Department or Graduate Program Coordinator

Abstract

Studies of the structural, electronic, and optical characteristics of the interfaces between graphene and ZnO polar surfaces is carried out using first-principles simulations. At the interface, a strong van der Waals force is present, and because of the different work functions of graphene and ZnO, charge transfer takes place. Graphene's superior conductivity is not impacted by its interaction with ZnO, since its Dirac point is unaffected despite its adsorption on ZnO. In hybrid systems, excited electrons with energies between 0 and 3 eV (above Fermi energy) are primarily accumulated on graphene. The calculations offer a theoretical justification for the successful operation of graphene/ZnO hybrid materials as photocatalysts and solar cells. ZnO semiconductor is found to be a suitable material with modest band gap, ($\sim$ 3 eV), having high transparency in visible region and a high optical conductivity.

Acknowledgment

First and foremost, I would want to express my profound gratitude and thanks to our Almight God for providing me with the courage and hope I needed to continue thinking that my thesis work would be achievable and more interesting. I want to convey my profound gratitude to **Dr. Kenate Nemera**, my adviser and instructor, for giving me the chance to work with him. His thesis-writing strategy has always pushed and inspired me to learn more. I will always benefit from his lectures on various aspects of computational material science. In addition, I want to thank him for his encouragement while we talked in class about certain material connected to my research title and the DFT idea. I wish him happiness, elegance, and success for the rest of time. Thanks also to my friends and classmates (Modelling and simulation of novel materials field students) for their support, encouragement, and helpful discussion. Last but not least, I want to express my love and gratitude to my beloved wife **Adey Mekonnin** and my son **Firaol Hailu** for their understanding, support, and love through the duration of my studies. I also express my sincere thanks to physics department of Addis Ababa University for facilitating conditions for specialization master in physics. Finally, I acknowledge Oromia Education Bureau for sponsoring me to work for my MSc degree in Physics, within specialized area of Modelling and Simulation of novel materials.

Contents

List of Figures

List of Tables

Chapter 1

Introduction

The ultimate spintronics device can be thought of as the interface between materials since it allows for new design possibilities and physical features that are not possible in the individual bulk materials [1]. Rashba-Edelstein spin-to-charge conversion and spin-momentum locking at the surface of topological insulators are two emerging interfacial phenomena caused by spin-orbit coupling (SOC). Interfaces naturally break spatial inversion symmetry, which causes an electronic band Rashba SO splitting that is often higher than in bulk. In particular, SO effects at oxide interfaces are crucial for low-power spintronics applications due to the expected long carrier lifetime and high Rashba coefficient [2]. Carbon-based nanomaterials are prime candidates for spin-based devices, due to their long spin coherence length (up to $10^4\ ps$) and high Fermi velocity [3]. Since the successful exploitation of single-layer graphene in 2004 by Geim and his co-workers [4], the investigations on the interaction of graphene and other nanomaterials have become a growing trend due to the extraordinary properties of graphene, such as the Dirac electrons near the K point, room-temperature quantum Hall effect, and high mobility of carrier electrons [5]. Research on the interaction of graphene with BN [6], SiC [7], metals [8], or metal oxides [9] has been done both experimentally and computationally thus far. The study of graphene-based interfaces is of great importance in materials production [10], device fabrication [11], and electrical measurement [12], because the contact of other materials with graphene may modify the physical and chemical properties of graphene and then influence its performance in devices.

In recent years, zinc oxide (ZnO) has attracted great attention in the field of nanodevices as an important semiconductor because of its unique optical, electronic, and magnetic properties, including large excitation binding energy (60 meV), wide band gap (3.4 eV), and unique piezoelectric properties [13]. A review of the literature reveals that the wide band gap, $>$ 3 eV, ZnO semiconductor is a suitable material with great transparency in the visible region and good optical conductivity. Some of ZnO properties are improved when it is synthesized in the form of nanosized material and, for this reason, a wide range

of ZnO nanostructures have been lately obtained [14] such as nanohelixies, nanobows, nanorings, nanowires, and nanocages, which are promising candidates for gas sensors, solar cells, field effect transistors, photocatalysts, and so on [15].
These materials display unique features such as greater photovoltaic properties than graphene or bulk ZnO alone in solar cells [16] and photocatalysts [17]. Despite the varied morphologies of graphene hybridizations with ZnO nanoparticles and vertical nanostructures, it is generally accepted that graphene's high specific surface area facilitates the loading of dyes in photocatalysis, and that charge transfer processes that involve charge-hole separation and transfer from graphene to ZnO are facilitated by graphene's higher conductivity. With significant experimental advancement, a computational investigation of graphene-ZnO hybrid systems has also been carried out [18]. In this work, the structural, interaction, and electronic properties of graphene-ZnO hybrid systems were investigated through density functional theory (DFT) computations to better understand the experimental results and hidden mechanisms.

1.1 Statement of the Problem

We need highly efficient, low-cost, and renewable energy sources. Solar cells which directly convert sunlight into electricity are promising candidates for commercialization on a large scale. Heterojunctions made up of two different types of donor and acceptor semiconductors were suggested as a viable method for the design of extremely efficient solar cells. But for a high-quality heterojunction solar cell, the donor and semiconductor must both have a direct band gap to absorb solar radiation, a high carrier mobility to encourage efficient electron transport, and a high stability in ambient conditions. The dependency on donor and acceptor semiconductors makes it necessary to look for suitable materials with ideal band gap, high carrier mobility, and high stability.
For nano- and opto-electric applications, it is very desirable to engineer a material's electrical properties. Particularly, its band gap, and strain is one method for doing this. Due to their ability to take substantially higher strain than bulk materials, 2D materials such as mono- and few-layer transition Metal Dichalcogenides (TMDCs) are ideal for flexible electrical and optoelectronic devices as well as strain-engineered materials. The idea of strain engineering for increasing the carrier mobility of 2D TMDCs is also quite intriguing. Effective electron-hole separation is required in solar cells, and this heavy charge separation not only makes it easier for excitons to split into free electrons and holes but also significantly reduces the rate at which electrons and holes recombine, potentially lengthening the lifetime of the minority carrier. Within a solar cell, photo-generated charging carriers must be divided. Two-dimensional (2D) materials have substantially developed up to this point due to their extensive variety of applications in catalysis, electrochemical energy storage, photocatalysis, optoelectronics, spintronics, and pho-

tonic nanodevices. Given their intriguing characteristics, TMDCs have drawn a lot of interest from these.

1.2 Significance of the Study

The results of this study is expected to be useful in:

- solar cell manufacturing industries to design solar cell experimentally.
- be a preliminary base for future research works related to novel properties of graphene-ZnO hetrojunction interfaces for a use in solar cell applications.

1.3 Objectives

1.3.1 General objectives

The main objective of this study is to systematically examine the novel properties of Graphene/ZnO hetrojunction interface for solar cell application using DFT + U + D2, as implemented within Gpaw code.

1.3.2 Specific objectives

The specific objectives of this research are:

- To perform the electronic property analysis for bulk ZnO and graphene/ZnO interface heterostructures.
- To evaluate the stable and efficient heterostructure configurations for photovoltaic applications.
- To investigate the prospect of photo-generated electron-hole pair recombination, calculate density of states, projected density of states, and work functions.

1.4 Organization of the thesis

This thesis has five chapters. Chapter 1 presents some generalities and motivation for studying of graphene-ZnO interface heterojunction. Chapter 2 presents a literature review description of novel heterojunction systems, and density functional theory. Chapter 3 describes details of numerical implementations and modeling. Chapter 4 describes the results obtained from the calculations using DFT within the Gpaw code. Chapter 5 presents conclusion of the current work, and recommendations for future works.

Chapter 2

Literature Review

2.1 Density Functional Theory

2.1.1 Introduction

In condensed matter theory and materials science, first-principles techniques based on density functional theory (DFT) [19–21] are powerful tools for predicting materials properties. When compared to experimental data, DFT can produce trustworthy and acceptable results for a number of materials properties. The ability of DFT to foresee changes in materials characteristics, on the other hand, is also its strength. As a result, DFT can assist production designers in predicting new materials with improved properties. DFT is extensively used as the basis theory in today's computational material science. This section briefly introduces the concept of DFT. The many-body Schrödinger equation has the physical knowledge that we require, but its application is restricted by our ability to discover a realistic description of the many-body effects contained in the exchange-correlation functional. It will be a precise theory if we have a comprehensive comprehension of this functional of DFT. In recent years, various exchange-correlation functional have been developed and successfully used in simulation calculations [22]. More details will be given in the following discussions.

2.1.2 Hamiltonian of Electronic system

The foundation of first-principles method relies on quantum mechanics that describes the behavior of electrons and atomic nuclei in any situation [23]. The Schrodinger equation serves as the basic equation in this topic, which can be expressed as follows, in Eq. (2.1),

$$\hat{H}\Psi = E\Psi \tag{2.1}$$

where $\hat{H}$ is the Hamiltonian operator, Ψ is the wavefunction, and E represents the energy of the system. The Hamiltonian operator consists of kinetic and potential energies due to the Coulombic interaction between electrons and nuclei as follows, Eq. (2.2),

$$\hat{H} = -\frac{\hbar^2}{2M_I}\sum_I \nabla_I^2 - \frac{\hbar^2}{2m_i}\sum_i \nabla_i^2 + \frac{1}{8\pi\varepsilon_0}\sum_{I\neq J}\frac{Z_I Z_J e^2}{|R_I - R_J|} - \frac{1}{4\pi\varepsilon_0}\sum_{I,i}\frac{Z_I e^2}{|R_I - r_i|} + \frac{1}{8\pi\varepsilon_0}\sum_{i\neq j}\frac{e^2}{|r_i - r_j|} \tag{2.2}$$

where $\bar{h}$ is the Planck's constant, e is the electron charge, Z_I is the charge of the nuclei, M_I is the mass of I^{th} nuclei, and m_i is the mass of i^{th} electron. Therefore, the contributions to the Hamiltonian comes from the kinetic energy T of nuclei and electrons (the first and second terms) and the potential energy due to the Coulomb interactions of nuclei-nuclei (namely V_{IJ}), nuclei-electron (namely external potential V_{ext}), and electron-electron (namely V_{e-e}), respectively. Apparently, the Schrödinger equation is too complex to be solved and would lead to uncontrollable computation in a system containing more than one electron. This is largely due to the nature of electrons that strongly interact which each other, which leads to many-body problem [23, 24]. Several approximations are then developed to solve the Schrödinger equation, of which the first useful one is the well-known Born Oppenheimer approximation [25].

2.1.3 Born-Oppenheimer Approximation

The idea in Born-Oppenheimer approximation is that the electron motion and nuclear motion are separated. This is due to the fact that the mass of the nucleus is way larger than that of the electron, and the nuclei are principally fixed particles. By having this approximation in mind, the problem of interacting electron, ions, and nuclei vanishes and eventually enables the possible application of the Schrödinger equation in a complex system. The Hamiltonian of the simplified (just electronic) system thus becomes

$$\hat{H} = -\frac{\hbar^2}{2m_i}\sum_i \nabla_i^2 - \frac{1}{4\pi\varepsilon_0}\sum_{I,i}\frac{Z_I e^2}{|R_I - r_i|} + \frac{1}{8\pi\varepsilon_0}\sum_{i\neq j}\frac{e^2}{|r_i - r_j|} \tag{2.3}$$

2.1.4 Hartree-Fock Method

In order to find the ground state wave function one basically has to minimize the functional $E\Psi$ with respect to all allowed N-electron wave functions. The Hartree-Fock (HF) approximation is a fundamental concept in quantum chemistry [26] that makes use of the variational principle. Instead of searching through all possible N-electron wave functions (which is impossible), it considers only a subset of wave functions. The total N-electron wave function is approximated as an anti-symmetrized product of N one-electron wave functions. As a result, the wave functions of the system with multi-electrons can be described as product of wavefunctions of single electron. This wave function of exchange potential is expressed by Hartree-Fock equation in Eq. (2.4) and this equation determines the set of (spin) orbitals with minimum energy and give us the best single determinant.

$$\Psi_{HF}(r_1, r_2, ..., r_N) = \frac{1}{\sqrt{N!}} \begin{pmatrix} \Psi_1(x_1) & \Psi_2(r_1) & \cdots & \Psi_N(r_1) \\ \Psi_1(r_2) & \Psi_2(r_2) & \cdots & \Psi_N(r_2) \\ \vdots & \vdots & \vdots & \vdots \\ \Psi_1(r_N) & \cdots & \cdots & \Psi_N(r_N) \end{pmatrix} \tag{2.4}$$

The HF hamiltonian in atomic units is:

$$\hat{H} = -\frac{1}{2}\sum_{i=1}^{N} \nabla_i^2 + V_{ext} + \sum_{i<j} \frac{1}{|r_i - r_j|} = T + V_{ext} + V_{coul} + V_{xc} \tag{2.5}$$

V_{ext} is called the external potential or electron-nuclei potential. Recall that the major expense in the HF approach is the calculation of exchange (and even more so is correlation). Instead of calculating using explicit exchange, DFT uses an additional function of the density, V_{xc}, where the x stands for exchange and the c stands for correlation. In 1964, Hohenberg and Kohn [19] have developed a theorem that defined the electron density as a unique function for ground state energy of a system of electrons. Later, a set of independent-electron equation has been established by Kohn and Sham [20]. They have introduced a Schr$\ddot{o}$dinger-like equation with a modified effective potential that is much easier to calculate than the original Schr$\ddot{o}$dinger equation.

2.1.5 The Hohenberg-Kohn theorems

There are two theorems formulated by Hohenberg and Kohn which served as the basis for modern DFT. The first theorem stated that in a system with N interacting electrons, the many-body ground state wavefunction, $\Psi(r_1, r_2, \cdots, r_n)$, of all electrons is a unique functional of the electron density, $\rho(r)$. It could be expressed in terms of position vector of electron, r, as follows, Eq. (2.6),

$$n(r) = \int \cdots \int |\Psi(r_1, r_2, \cdots, r_n)|^2 dr_1 dr_2 \cdots dr_n \tag{2.6}$$

As the Hamiltonian equation is comprised of the sum of electronic kinetic energy T, attractive electron-nuclear V_{Ne}, and electron-electron repulsions V_{ee}, the molecular property based on these average variables are determined by ground state electronic wavefunction $\rho_0(r)$. The total energy is calculated as follows, Eq. (2.7),

$$E_0 = E_v[\rho_0] = \bar{T}[\rho_0] + \bar{V}_{\text{Ne}} + \bar{V}_{\text{ee}}[\rho_0] \tag{2.7}$$

where overbars denote the average variables. By considering $V(r)$ as a function of r for nuclear potential energy for an electron at point r, the Hohenberg-Kohn equation can be expressed as follows (Eq. (2.8)):

$$E_0 = E_0[\rho_0] = \bar{T}[\rho_0] + \bar{V}_{\text{ee}}[\rho_0] + \int \rho_0(\mathrm{r})\mathrm{V}(\mathrm{r})\mathrm{dr} \tag{2.8}$$

The first theorem focuses on the wavefunctions and energy functional. The second Hohenberg-Kohn theorem allocates a minimum principle for the density. It stated that the ground state energy of any trial electron density cannot be smaller than the true ground state system, Eq. (2.9),

$$E[\rho] = E \geq E_0 \ = \ E_0[\rho_0] \tag{2.9}$$

2.1.6 Kohn-Sham method

The Kohn-Sham method introduced a fictitious supporting system to resemble the true many-electron system. This approach gives a set of independent electron equations that are numerically solvable. The total energy is now calculated as follows, Eq. (2.10),

$$E[\rho] = \int \rho(r)V(r)dr + \bar{T}_s[\rho] + \frac{1}{2}\int\int \frac{\rho(r_1)\rho(r_2)}{r_{12}}dr_1dr_2 + E_{xc}[\rho] \tag{2.10}$$

E_{xc} is known as the exchange-correlation energy that contains the correlation energy, exchange energy, Coulombic correlation energy, and self-interaction correction. So far, no exact expression for this exchange and correlation (XC) potential is known [27]. An approximation is thus embodied in the formalism to ensure the accuracy of DFT calculation approximations conveys different definitions and approaches, and is thus suitable for specific materials. Among them, the LDA and GGA are the ones widely used in DFT calculation of ZnO system [5, 19, 23, 25, 28–31].

2.1.7 Exchange-Correlation functional

We will look at numerous exchange-correlation approximations in this section, including Local Density Approximation (LDA), Generalized Gradient Approximations (GGA), and PBE. The spin-unpolarized instances are the focus of the following discussion.

Local Density Approximation (LDA)

The idea of LDA is that for a given region of material with a slow varying in charge density, the XC energy at point r is only dependent on the particle density $n(r)$ at that point [32]. This XC energy must be similar to homogeneous electron gas (e^{hom}) of the same charge density. The LDA formalism is presented as follows, Eq. (2.11),

$$E_{xc}^{LDA}[n(r)] = \int n(r)e_{xc}^{hom}[n(r)]dr \tag{2.11}$$

To date, the LDA has successfully calculated the properties of metal, insulator, and semiconductor of materials with predictive accuracy [33]. LDA was also found to be very efficient in the extended system, such as calculation in solids and large molecules [27]. However, the localized characteristic in LDA has enabled the incorrect treatment of electronic structure of certain materials, especially in a system with strongly correlated structure [28, 32, 34]. ZnO is an example of a strongly correlated structure owing to the full electrons at Zn-3d state which make the electrons to behave more like a core and have a strong correlation with atomic nuclei.

Generalized Gradient Approximation (GGA)

The extension to improve the accuracy of LDA is provided by second approximation known as GGA. This formalism uses two variables instead of one variable as in LDA (the density), which are the electron density and its gradient, as given by the following equation, Eq. (2.12),

$$E_{XC}^{GGA}[n(r)] = \int n(r)e_{XC}^{hom}[n(r), \nabla n(r)]dr \tag{2.12}$$

In addition, several corrected functionals are developed in GGA formalism to include the contribution of exchange and correlation part. These functionals are PBE, PBESol [35], and Perdew-Wang (PW91).

PBE

The PBE exchange-correlation functional can be expressed as

$$E_{XC}^{PBE} = \int n(r)\varepsilon_{XC}^{LDA}[n]F_{XC}^{PBE}(r_s, s)dr \tag{2.13}$$

Where F_{XC}^{PBE}=$F_X^{PBE}(s)$ + $F_C^{PBE}(r_s, s)$ denotes the PBE enhancement factor. PBE functional satisfies some conditions of the inhomogeneous electron gas. Theoretically, GGA PBE provides more accurate features than LDA. For PBE exchange functional, the enhancement factor is given by

$$F_X^{PBE}(s) = 1 + K - \frac{K}{1 + \frac{\mu}{K}s^2} \tag{2.14}$$

2.1.8 Hubbard scheme (DFT+U)

The remedy for shortcoming calculation error of LDA and GGA in ZnO system has long been discussed and proposed. There is a method known as scissor operator incorporated in computer code to increase the band gap [36], self-interaction correction (SIC) [30, 33], and Hubbard-U correction [37]. Among them, Hubbard-U method is widely used as its calculation procedure is simple, the calculated results are reliable, and it is practically economical. On this basis, the Hubbard-U method pioneered by Anisimov et al. [38] introduced an orbital-dependent term known as on-site Coulomb repulsion energy, U, into the XC term of LDA and GGA. They are now referred to as LDA + U or GGA + U and expressed as follows, Eq. (2.15),

$$E_{LDA+U}[n(r)] = E_{LDA}[n(r)] + E_U[n(r)] - E_{dc} \tag{2.15}$$

Here, $n(r)$ is the electron density, $\mathrm{E_{LDA}}$ is the energy from conventional LDA functional, E_U is the Hubbard type energy, and E_{dc} is the double-counting correction energy. Depending on the computer program, the Coulomb energy U and the exchange energy J are combined into a single parameter known as on-site Coulomb repulsion U, which been used in Cambridge Serial Total Energy Package (CASTEP) computer code [36]. The on-site Coulomb interactions are particularly strong for localized $d + f$ electrons but can also be important for p localized orbit [32, 39]. Hence, LDA + U or GGA + U had potentially improved the insufficient description of strongly localized electrons, such as those in Zn-3d state, which is previously not correctly described in LDA and GGA.

2.1.9 The Bloch Theorem

To do DFT calculations on infinite systems, one must first assume that the system's structure is homogeneous in all directions and then apply periodic boundary conditions (pbc). We introduce a supercell for the set of coordinates of atomic nuclei, which involves a periodically repeating pattern of atoms fulfilling translational symmetry criteria. The Bloch theorem [40] states, that the eigenvalues in a periodic solid have the form

$$\Psi_{\mathrm{n,k}}(\mathrm{r}) = \mathrm{e}^{\mathrm{ik.r}}\mathrm{u}_{\mathrm{n,k}}(\mathrm{r}) \tag{2.16}$$

where n is the "$band\ index$" and k is a wave vector confined to the first Brillouin zone of the reciprocal lattice. u_k is translationally invariant, i.e.,

$$u_{\mathrm{n,k}}(\mathrm{r}+\mathrm{T}) = \mathrm{u_{n,k}(r)} \tag{2.17}$$

where T is a translational vector of the crystal lattice. Eigenstates of this form are called Bloch functions. Wave functions Ψ_{nk} and their eigenvalues are periodic in k-space,

$$\Psi_{\mathrm{n,k+G}}(\mathrm{r}) = \Psi_{\mathrm{n,k}}(\mathrm{r}),\ \text{and } \mathrm{E_{n,k+G}(r) = E_{n,k}(r)} \tag{2.18}$$

where G is an arbitrary reciprocal lattice vector. Hence it is sufficient to consider them and their eigenvalues only in the first Brillouin-zone. Deriving the Schr$\ddot{o}$dinger equation with Bloch functions yields an equation for a periodic function $\Psi_\mathrm{k}(\mathrm{r})$. Using periodic boundary conditions leads to a Hermitian eigenvalue equation over the Wigner-Seitz cell in the crystal. For a fixed k, there is an infinite number of solutions with rising energy values.

2.1.10 Plane waves and Pseudo-potentials

The electron orbitals used to express the single particle states may be expanded interms of any convenient basis set. In practice, a plane wave basis set

$$\Psi^n_k(r) = \sum_G C^{n,k}_G e^{i(k+G).r} \tag{2.19}$$

based on the Bloch theorem is used with a following benefits.

- A plane wave basis set is unbiased, it does not assume any preconceptions on the form of the problem.
- Due to Bloch theorem, plane waves are the natural choice for the representation of electron orbitals in a periodic system.
- The kinetic energy operator is diagonal in a plane wave representation. Similarly, the potential is diagonal in real space. The use of Fast Fourier Transforms (FFT) in changing between these representations provides a large saving in computational cost.

The number of plane wave basis functions needed to adequately characterize atomic wave functions near a nucleus would be massive. This problem is solved by using pseudopotentials [41], which represent the ionic cores potential. This approximation is based on the premise that the physical and chemical properties of the system are influenced only by the valence electrons. The pseudopotential represents the nuclie's and core electrons' potentials under the following conditions.

- The valence wavefunction remains unchanged outside the core region (beyond r_c boundary).
- The pseudo wavefunction, as well its first derivative, must be continuous at the boundary (see Eq. (2.20)).

  $$\Psi^{ps}(r)|_{r=r_c} = \Psi^{AE}(r)|_{r=r_c} \; and \; \frac{\partial}{\partial(r)}\Psi^{ps}(r)|_{r=r_c} = \frac{\partial}{\partial(r)}\Psi^{AE}(r)|_{r=r_c} \tag{2.20}$$

  The indices PS and AE stand for pseudo and all-electron energies, respectively.
- The pseudo wavefunction is nodeless within the core region.

Figure 2.1, taken from reference [42] shows a graphical representation of the behavior of a wave function and potential. For the pseudo-potential to be useful, all of the above mentioned basic criteria must be meet. For the construction of other types of pseudo-potentials, such as ultra-soft (or Vanderbilt) pseudo-potentials (USPP), norm conserving pseudopotentials (NCPP), and so on, additional criteria must be included. P.Bloch [40] created the so called projector augmented wave method (PAW) [43] as an enhancement on the pseudo-potential technique approach. It is based on the all-electron wavefunction

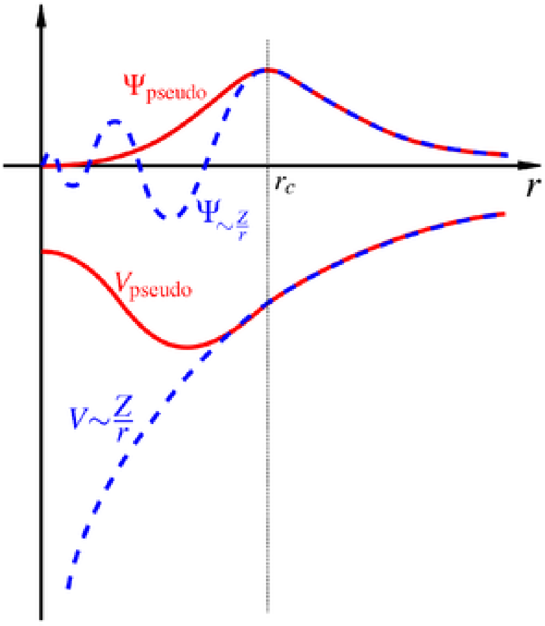

Figure 2.1: Comparison of a wavefunction in the Coulomb potential of the nucleus (blue) to the one in the pseudo-potential (red). The real and the pseudo wavefunction and potentials match above a certain cutoff radius (core radius) r_c. The cut-off vector is G_{max} in this case.

being transformed from the pseudo-wavefunction. The Ψ all electron wavefunction is made up of three parts:

$$\Psi = \tilde{\Psi} + \sum_{i}^{N} c_i \Phi_i - \sum_{i}^{N} c_i \tilde{\Phi}_i \tag{2.21}$$

where $\tilde{\Psi}$ is the pseudo-wavefunction, Ψ_i are the all-electron partial waves and $\tilde{\Phi}_i$ are the pseudo partial waves. A tilde is used to distinguish between the all electron (AE) quantities and the pseudo (PS) quantities. The PS wave function is represented by plane waves that are a decent representation of the wave function far away from the nuclei, but deviates greatly from the AE wave function near the nucleus. To address this discrepancy, the AE partial waves Φ_i are introduced. These AE partial waves are calculated once as isolated atom solutions to the radial component of the Schr$\ddot{o}$dinger equation. They differ from the PS wave function inside the so-called augmented (core) region, but they match outside this region. The AE partial waves verify that the wave function's nodal structure around the nucleus is physically proper. Because this region is already included in the AE partial waves, the contribution of the PS partial waves, $\tilde{\Phi}_i$, which are located near the atomic nuclei, is subtracted from the PS wave function. The $\tilde{\Phi}_i$ partial waves are built similarly to the AE partial waves as solutions of the radial Schr$\ddot{o}$dinger's equation for isolated atoms fitted to the PS wave function.

2.1.11 Plane wave cut-off energy and K-points

In the unit cell, the Hamiltonian of Kohn-Sham is periodic. The wave functions might be of the plane wave type (Bloch wave function), which looks like,

$$\Psi_{\mathrm{nk}}(\mathrm{r}) = \mathrm{e}^{\mathrm{ik.r}} \mathrm{u}_{\mathrm{nk}}(\mathrm{r}) \tag{2.22}$$

where k represents the wave vector and n represents the energy band. A sum over reciprocal lattice vector G with k belonging to the first Brillouin Zone (BZ) is given as:

$$u_{\mathrm{nk}} = \sum_{\mathrm{G}}^{\mathrm{G_{max}}} \mathrm{c}_{\mathrm{nk}} \mathrm{e}^{\mathrm{iG.r}} \tag{2.23}$$

The more accurate the representation of the wave function is when the plane wave basis is larger and the norm of vector G is increased. As a result, increasing G is used to order the expansion. It reaches a finite number of reciprocal lattice vectors before truncating. For a given k, the G satisfies;

$$\frac{\hbar^2}{2m} |k + G|^2_{cut} \leq E_{cut} \tag{2.24}$$

where E_{cut} is the plane wave cut-off energy which is given by:

$$E_{cut} = \frac{\hbar^2}{2m} G_{cut}^2 \tag{2.25}$$

With an acceptable cut-off energy for the plane wave basis set, the plane wave calculation was carried out. The energy cut-off and the number of k-points in the Brillouin zone are two key factors that must be carefully chosen in electronic structure computations of bulk ZnO. Prior to running production runs, best practices in this industry often require a convergence analysis of the amount of interest in relation to these factors. As a result, the total energy has been verified for convergence with regard to the energy cut-off and the number of k-points. In this work, the energy cut-off value of 400 eV is chosen, while an $8 \times 8 \times 8$ k-mesh were used to sample k-points of the Brillouin zone. The k-points are generated based on Monkhorst-Pack scheme.

2.1.12 Analysis of the Electronic Properties

Computational materials science gives researchers a powerful tools for examining electronic structure and properties. A couple of these will be discussed below, particularly the density of states and charge density analysis.

Density of States (DOS) and projected density of states (PDOS)

The density of states (DOS) describes number of states per unit of energy E (and per unit of volume in extended matter) is an essential property for many applications [44],

$$n(E) = \frac{1}{N_k} \sum_i \sum_k \delta(\varepsilon_{i,k} - E) = \frac{\omega_{cell}}{(2\pi)^d} \int_{BZ} \delta(\varepsilon_{i,k} - E) dk \tag{2.26}$$

In the case of independent-particle states, $n(E)$ from Eq. (2.26) is the number of independent particle states per unit energy, whereas, $\varepsilon_{i,k}$ represents the energy of an electron (or phonon). In theory, calculating the integral in Eq. (2.24) is not a simple operation. The linear tetrahedron technique (LTM) by Jepsen and Andersen [45], the modified tetrahedron approach (MTM) by Bloch et al [46], and the Gaussian broadening method (GBM) by Methfessel and Paxton [47] are three common types of methods for this Brillouin zone integration. The projected density of states (PDOS) is defined by

$$n(\alpha, E) = \sum_i \sum_k | < \Psi_{\alpha k}(r) | \Psi_{ik}(r) > |^2 \delta(\varepsilon_{i,k} - E) \tag{2.27}$$

where $\Psi_{\alpha \mathrm{k}}$ denotes orthonormal states to Ψ_{ik}. The PDOS is a DOS projection onto atomic orbitals, in principle. At absolute zero temperature, the Fermi Energy E_F is the energy of the highest occupied quantum state in a system of fermions. Because the Fermi energy E_F appears in all DOS / PDOS spectra, it is often intentionally made to coincide with the zero energy level by shifting the energy levels from E to $E - E_F$.

2.1.13 Charge Density

The charge density $\rho(r)$ is an important physical quantity obtained from first-principles calculations based on density functional theory (DFT). Much useful information about the investigated materials can be extracted from it, such as chemical bonding, charge transfer, and orbital hybridization. Charge density depends on the position vector r and is a spatial charge distribution over the volume of a molecule or a unit cell of a periodic solid. The electronic charge density is thus given by the equation

$$\rho(r) = e\sum_{nk}^{occ} |\Psi_{\mathrm{nk}}(\mathrm{r})|^2 = \mathrm{en(r)} \tag{2.28}$$

where e is the electron's charge (e = 1.6021733 × 10^{-19} Coulomb), Ψ_{nk}(r) is the n^{th} band's wave function, and the sum extends to over all occupied electronic states. The electron density, given by,

$$n(r) = \sum_{nk}^{occ} |\Psi_{\mathrm{nk}}(\mathrm{r})|^2 \tag{2.29}$$

can be visualized by plotting 3D isosurfaces (a surface for a discrete isovalue) or 2D contour plots (a set of isocontours).

2.1.14 Geometry Optimization

Finding the system's electronic ground state, the precise configuration of atoms that corresponds to the lowest potential energy is essential in performing ab-initio calculations. When searching for the ideal arrangement of atoms, the quantum-mechanical code undertakes several ionic relaxation steps, which involves moving all of the nuclei in the proper direction (along energy gradients) such that each nucleus has a lower potential energy. After each ionic step, a self-consistent cycle of electronic relaxation stages must be employed to calculate the ground state energy. When the energy gradients (or forces on atoms) are smaller than pre-defined tolerance values, the geometry optimization process stops & a final self-consistent cycle of the electronic relaxation must be employed to calculate the ground state energy of the final atomic arrangement. The numerical algorithms listed below are commonly employed in ab-initio codes to find the ground state energies based on energy and gradients.

- Conjugate-gradient (CG) method.
- Residual minimization method (RMM)

- Quasi-Newton method
- Variable metric method (BFGS)

2.2 Structural, electronic, and optical properties of graphene

2.2.1 Structural properties of graphene

Graphene is a single atomic layer of carbon atoms. The carbon atoms are sp^2-hybridized and therefore are arranged in a hexagonal crystal lattice. This schematically structure is shown in Fig. 2.2. The atomic structure of graphene can be compared with chicken wire or a honeycomb. This structure was confirmed, for example, by scanning tunneling microscopy (STM) [48]. The bond length between two carbon atoms in graphene is about 0.142 nm. Although considered as a flat sheet, graphene is actually rippled. Experimental observation [49] and theoretical calculations [50] show an out-of-plane deformation of about 1 nm. The lateral size distribution of these ripples is 50-100 nm. These ripples may be the reason that relatively large graphene sheets are stable at all. They can be seen as a mechanism to lower the thermal vibrations that threaten the stability of all two-dimensional layers. Graphene can be considered as the base material from which other sp^2 carbon allotropes can be folded. The interlayer spacing in stacks of multiple layers is 0.335 nm. The layers in few-layer graphene (FLG) and graphite are held together by weak van der Waals forces.

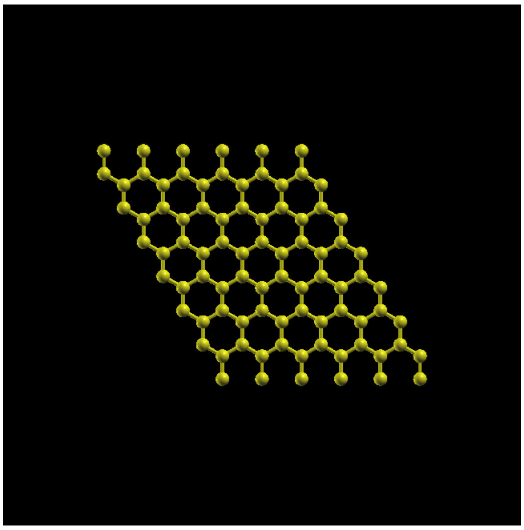

Figure 2.2: Structural properties of graphene.

2.2.2 Electronic properties of graphene

The electronic properties of graphene have opened new doors in physics and they are often described as exotic and unique. Charge carriers in graphene cannot be described with regular nonrelativistic quantum mechanics and the Schr$\ddot{o}$dinger equation. They obey the rules of relativistic quantum mechanics also called quantum electrodynamics (QED). Charge carriers in graphene are described as massless Dirac fermions. This type of physics could be observed only in cosmology and high-energy particle accelerators. With the discovery of graphene, however, these phenomena of quantum electrodynamics can be studied in the laboratory. For now, graphene is the only solid known to exhibit these quantum electrodynamics [51]. This is partly due to the fact that graphene can be produced or isolated with exceptional crystalline quality. Other existing 2D materials lack this electronic quality. A single graphene layer is a zero-gap semiconductor. The electronic band structure of graphene is determined by its orbitals. The valence and conduction bands touch each other at the K points, also called Dirac points. These K points are the corners of a two-dimensional hexagonal Brillouin zone. There are actually three K points and three K points linked to the two sublattices of graphene. The low energy band structure around these K points resembles two touching cones with a linear energy-momentum (E-k) dispersion relation. The dispersion relation is given by the following equation:

$$E = |\hbar.k|\nu_f \tag{2.30}$$

where $\hbar.k$ is momentum and ν_f is the Fermi velocity. The Fermi velocity in this case is $10^6\ ms^{-1}$, which is 300 times slower than the speed of light. A consequence of this linear dispersion relation is that the charge carriers behave as massless particles [52–54].

2.2.3 Optical properties of graphene

Free standing graphene has an optical transmittance of 97.7$\%$ and a reflection of less than 0.1$\%$. Furthermore, the optical transmittance is independent of wavelength [28]. Graphene has an absorption coefficient of 301.66 cm^{-1} [30] and a complex refractive index of $n = 2.0 - i\ 1.1$ in the visible range [31]. The opacity or absorption of 2.3 $\%$ of white light is relatively high for a single atomic sheet. This is the result of graphene's unique electronic properties.

2.3 Crystal Structure, electronic and optical properties of ZnO

2.3.1 Crystal structure of ZnO

The crystal structures showed by ZnO are hexagonal wurtzite (B4), cubic zinc-blende (B3), and cubic rocksalt (or Rochelle salt) (B1) depending on the applied pressure.

Cubic Zinc-blende structure of ZnO

Only heteroepitaxial development on cubic substrates like ZnS can sustain the metastable cubic zinc-blende ZnO structure. Based on current ab-initio techniques, it is projected that the computed lattice constants for the zinc blende poly-type of ZnO will be 4.60 Å and 4.62 Å. The cubic zinc-blende structure is made up of two interpenetrating face-centered cubic (fcc) sublattices that are moved by one-fourth of the body diagonal and has symmetry determined by space group F43m in the Hermann-Mauguin notation, and T_d^2 in the Schoenflies notation [26]. The wurtzite and zinc blende structures differ only in the bond angle of the second-nearest neighbors and therefore, in the stacking sequence of close-packed diatomic planes.

Rock salt structure of ZnO

The lattice constant decreases to a range of 4.27-4.29 Å during the high-pressure phase transition from the wurtzite to the rocksalt structure. The rocksalt type of structure has a sixfold coordinated space group symmetry of Fm3m in the Hermann-Mauguin notation, and O_h^5 in the Schoenflies notation. However, epitaxial growth is unable to maintain the rocksalt structure [55].

Wurtzite structure of ZnO

Under ambient conditions, the thermodynamically stable phase is that of wurtzite symmetry. The wurtzite structure has a hexagonal unit cell with two lattice parameters a and c. These lattice constants mostly range from 3.25 to 3.25 Å for the a-parameter and from 5.20 to 5.21 Å for the c parameter. It belongs to the space group $C_{6\nu}^4$ in the Schoen flies notation, and $P6_{3mc}$ in the Hermann-Mauguin notation. In this case, each anion is tetrahedrally surrounded by four cations and vice versa. The schematically wurtzite structure of ZnO is shown in Fig. 2.3.

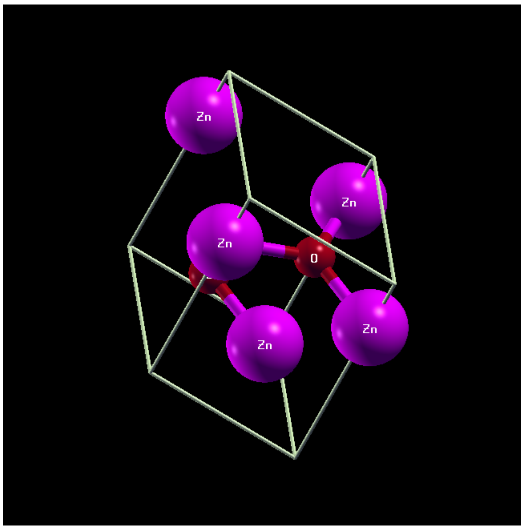

Figure 2.3: Wurtzite structure of ZnO.

2.3.2 Electrical properties of bulk wurtzite ZnO

ZnO has a relatively large direct band gap of ~ 3.4 eV at room temperature. Advantages associated with a large band gap include higher breakdown voltages, ability to sustain large electric fields, lower electronic noise, and high-temperature and high-power operation. The band gap of ZnO can further be tuned to $\sim 3-4$ eV by its alloying with magnesium oxide or cadmium oxide [56]. Most ZnO has n-type character, even in the absence of intentional doping.

Band structures and band gap of bulk wurtzite ZnO

Band structures are a representation of the allowed electronic energy levels of solid materials and are used to inform their electrical properties [57]. Band structure is the plot of the energies of electrons, eigenvalue energies $\varepsilon(k)$ against the k points. A band gap is a range of energy level in a material in which electrons cannot exist. The absence as well as its size can help us understand the electronic behavior of a material and distinguish electrical insulators, conductors, and semiconductors. The valence band and the conduction band are the two distinct areas of the band structure. If the band gap is "wide", materials are classified as insulators. The distinction between these two types of materials is arbitrary, however, band gaps greater than 3 eV are commonly referred to be wide band gaps. Metals are materials possessing a non-zero band structure at the Fermi level.

2.3.3 Optical properties of bulk wurtzite ZnO

Zinc oxide is noted for its strongly nonlinear optical properties, especially in bulk. The nonlinearity of ZnO nanoparticles can be fine-tuned according to their size [58]. The optical properties of a material can be described by means of the dielectric function $\varepsilon(\omega) = \varepsilon_1(\omega) + i\varepsilon_2(\omega)$. The imaginary part $\varepsilon_2(\omega)$ of the dielectric function is calculated using the following expression [59].

$$\varepsilon_2 = \frac{2e^2\pi}{\Omega\varepsilon_0} \sum | < \varphi_k^c|u.r|\varphi_k^v > |^2 \delta(E_k^c - E_k^v - \omega) \tag{2.31}$$

where e is the electronic charge; Ω is the unit cell volume; u is the vector defining the polarization of the incident electric field; ω is the light frequency; φ_k^v and φ_k^c are the wave functions of the conduction and valence band, respectively. The real part of the dielectric function $\varepsilon_1(\omega)$ can be calculated from the imaginary part $\varepsilon_2(\omega)$ using the Kramers-Kronig relation. The absorption coefficient $\alpha(\omega)$ can be obtained from $\varepsilon_1(\omega)$ and $\varepsilon_2(\omega)$. The relationship among the absorption coefficient, thin film thickness, and transmittance is calculated using the following expression

$$T = (1 - R)^2 e^{-\alpha d} \tag{2.32}$$

where T is transmittance; R is reflectivity; α is the absorption coefficient; and d is the thickness of the thin film, which was set at 250 nm.

The absorption coefficient $\alpha(\omega)$

The inter-band absorption coefficient $\alpha(\omega)$ characterizes the part of energy absorbed by the solid. It determines how far light, of a particular wavelength, can penetrate a material before it is absorbed. In a material with a low absorption coefficient, the light is only weakly absorbed, and, if the material is thin enough, it appears transparent for this wavelength. The absorption coefficient depends on the material and also on the wavelength of the light that is absorbed. It can be defined according to the extinction coefficient $K(\omega)$ by the following relation:

$$\alpha(\omega) = \frac{2\pi}{\lambda} K(\omega) \tag{2.33}$$

Where λ represents the wavelength of light in the vacuum. The absorption coefficient can be calculated via the dielectric function by the following relationship:

$$\alpha(\omega) = \sqrt{2}\frac{\omega}{c}\sqrt{\sqrt{\varepsilon_1^2(\omega) + \varepsilon_2^2(\omega)} - \varepsilon_1(\omega)} \tag{2.34}$$

In the light of $\varepsilon_1(\omega)$ and $\varepsilon_2(\omega)$ the electron energy-loss function defined as

$$L(\omega) = \frac{\varepsilon_2(\omega)}{[\varepsilon_1^2(\omega) + \varepsilon_2^2(\omega)]} \tag{2.35}$$

The electron energy loss function $L(\omega)$ is another useful tool to investigate the behavior of a material with the light. This property of a medium or a material measures the propagation loss of energy inside the medium or material.

The optical conductivity $\sigma(\omega)$

The occupied states are excited towards the unoccupied states above the Fermi level by the absorption of photons. This inter-band transition is called "optical conduction" and photon absorption is called "inter-band absorption". The term "optical conduction" means electrical conduction in the presence of the electric field from the light. The real part of the optical conductivity is calculated according to the following relation:

$$Re\ \sigma(\omega) = \frac{\omega}{4\pi} Im\ \varepsilon(\omega) \tag{2.36}$$

The optical constants $n(\omega)$ *and* $\mathbf{K}(\omega)$

The refraction causes the propagation of light waves with a velocity smaller than that in a free space (for example: air). The reduction in velocity leads to bending of the light rays at the interfaces, described by Snell's law of refraction. Refraction, in itself, does not affect the intensity of light during its propagation. The propagation of a light beam through a translucent medium is described by the refractive index n. The latter is defined by the relationship between the velocity of light in free space c and that in the medium v according to the relationship:

$$n = \frac{c}{v} \tag{2.37}$$

The refractive index depends on the frequency of the light beam. This effect is called dispersion. The refractive index $n(\omega)$ is calculated by the following relation:

$$n(\omega) = \frac{1}{\sqrt{2}} \sqrt{\sqrt{\varepsilon_1^2(\omega) + \varepsilon_2^2(\omega)} + \varepsilon_1(\omega)} \tag{2.38}$$

The extinction coefficient represents the energy loss (due to absorption and diffusion) in the medium, in the magnitude of the complex refractive index ($\tilde{n} = n + iK$), which characterizes any medium. So, it is linked to the absorption coefficient by the relationship described above. The extinction coefficient $K(\omega)$ is given by the following relation:

$$K(\omega) = \left| \frac{-\varepsilon_1(\omega)}{2} + \frac{\sqrt{\varepsilon_1^2(\omega) + \varepsilon_2^2(\omega)}}{2} \right|^{\frac{1}{2}} \tag{2.39}$$

At low frequencies, ($\omega = 0$), the relations of n and K becomes: $n(0) = \varepsilon(0)^{\frac{1}{2}}$, $K(0) = 0$. The refractive index represents the dispersion behavior of the material.

The reflection coefficient $R(\omega)$

The reflection phenomenon that occurs at the front and rear surfaces is described by the reflection coefficient which represents the ratio between the energy reflected and the energy incident on the surface. The reflection coefficient $R(\omega)$ is given by the following relation:

$$R(\omega) = \left| \frac{\sqrt{\varepsilon(\omega)} - 1}{\sqrt{\varepsilon(\omega)} + 1} \right|^2 \tag{2.40}$$

The modulus of the complex function $R(\omega)$ is also given by the following relation:

$$R(\omega) = \frac{(n-1)^2 + K}{(n+1)^2 + K} \tag{2.41}$$

2.4 Surface properties of clean wurtzite ZnO

For WZ structures, it is possible to calculate surface energies of symmetric non-polar surfaces, such as $(10\bar{1}0)$ and $(11\bar{2}0)$ surfaces by standard slab methods based on density functional theory approaches. However, it is impossible to apply this method to polar or semi-polar surfaces because of the absence of symmetry. Several attempts were made to calculate the polar surface energies of WZ ZnO [60] and GaN [61], based on a zinc blende (ZB)/WZ hetero-junction scheme. ZB based (111) or $(1\bar{1}1)$ surfaces are adopted as reasonable approximation to simulate the c and -c planes of WZ structure in the literature [60, 61]. This is because: (1) the formation enthalpies of ZB and WZ ZnO (or GaN) are similar; (2) the surface atoms on the ZB (111)/$(1\bar{1}1)$ planes have the same coordination and structures up to the 2nd nearest neighbors of the surface atoms as the WZ (0001)/$(000\bar{1})$ polar planes [61]. ZB-(111) and WZ-(0001) means cation-terminated surfaces and ZB-$(1\bar{1}1)$ and WZ-$(000\bar{1})$ denote anion-terminated ones. To improve the accuracies of the WZ calculations, it's important to have a highly accurate ZB results. The polar and non-polar surfaces of wurtzite ZnO is given in Fig. 2.4.

2.4.1 Surface energy of clean wurtzite ZnO

Due to the inability to decouple the two inequivalent (0001)-Zn and $(000\bar{1})$-O surfaces, it is challenging to calculate the precise surface energies for (0001) surfaces of wurtzite ZnO. We have approximated the surface energies to a high degree of accuracy by converting the uncertainty of the surface energies into that of the interface energies, which is substantially smaller than the former. Within the primary temperature and oxy-

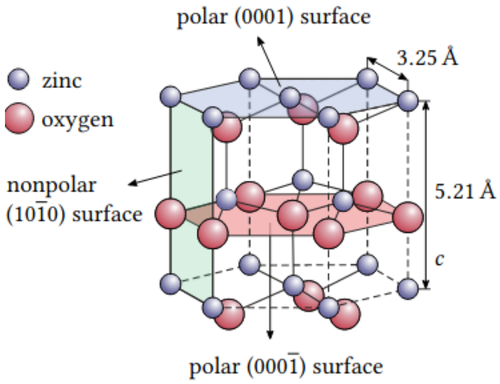

Figure 2.4: Geometric structure of wurtzite ZnO. The nonpolar $(10\bar{1}0)$, $(000\bar{1})$-O polar and (0001)-Zn polar surfaces are indicated. The direction of the c-axis is perpendicular to the polar surfaces.

gen partial pressure range available for experimentation, it is discovered that the oxygen terminated (000$\bar{1}$)-O face of the wurtzite phase and ($\overline{111}$)-O of the zinc blende phase are more stable than their Zn-terminated counterparts.

2.4.2 Work Function of clean wurtzite ZnO

The work function is the minimum energy needed to remove an electron from the bulk of a material through a surface to a point outside the material, and can be written as,

$$\Phi = V_{vac} - E_f \tag{2.42}$$

where V_{vac} is the potential in the vacuum region and E_f is the Fermi energy. In practice, this is the energy required at 0 K to remove an electron from the Fermi level of the oxide to the vacuum level [62]. Calculations of work function using DFT employ this definition and determine the Fermi energy and vacuum potential from calculations of the metals in slab supercell geometries. However, work functions calculated with slab approximations are known to have a dependency on the thickness of the slab, thus further analysis is required to extract bulk metal work functions from slab approximation. This dependency is well documented in some cases and is attributed to finite size effects arising from classical electrostatic interactions or from quantum size effects [63,64]. Methodology to lessen such effects is available in the literature [65]. It appears also necessary to analyze prospect of bulk vacancy formations. The vacancy formation energy E_{vac} [eV] is defined as

$$E_{vac} = E_v - \frac{N-1}{N} E_{bulk} \tag{2.43}$$

Adsorption by Ab-Initio Modeling

In nature, crystals are three-dimensional (3D) objects that end in surfaces [66]. Many phenomena and processes, including adsorption, can take place at the interface between a condensed phase and the environment. Surface modeling is of great theoretical and practical relevance. A surface can be created by cutting a crystal along a crystalline plane. As a result, surfaces have limitless two-dimensional atom configurations (2D). A slab model has been suggested while studying on surfaces in order to apply Bloch's theorem, which necessitates periodicity in all three directions.

2.4.3 Spin polarization

An essential characteristic of electron-electron interactions in electronic systems is spin polarization. An open-shell atom has unpaired electrons in its ground state, which allows it to carry a magnetic moment via spin polarization in valence orbitals. According to a nave theory, in order to maximize the decrease of the electron-election repulsion by making use of the Pauli exclusion principle, the magnetic moments would be aligned in parallel among neighboring atoms.

However, the double electron occupancy of bonding (delocalized) orbitals is favored by energy reduction through the creation of chemical bonds or electron delocalization, which results in an antiparallel spin alignment or even a spin unpolarized electronic structure. No one of two conflicting effects is consistently dominant in molecules and solids, according to observations of different magnetic behaviors. Understanding the competition and its effects, particularly in solid-state molecules, is difficult on two different levels. First, multiple magnetic compounds exist, and understanding their properties seems to require distinct conceptual foundations for each one. Second, various models for various forms of magnetism have been constructed with varying degrees of approximations and sophistications. A unified conceptual model known as "spin polarization perturbational orbital theory (SPPOT)" is presented in this chapter as an analysis of the conventional models [67].

Chapter 3

Methodology

3.1 Implementation of DFT

All calculations in this work were carried out using the GPAW code, where the detail of the capabilities is described in a literature [68]. The exchange-correlation energy of the interacting electrons is expressed using the frozen-core full potential projector augmented wave (PAW) approach [46] and the Perdew-Burke-Ernzerhof (PBE) form [35]. The electronic ground state was determined using the plane waves basis with a cut-off energy of 550 eV and the conjugate gradient algorithm, with the convergence threshold set at $5{\times}10^{-4}$ eV for energy and 0.01 eV/Å for force. The Brillouin zone integrations were carried out using Monkhorst-Pack grids [69].

We used k-point meshes of $6{\times}6{\times}6$ for a wurtzite ZnO primitive cell, $6{\times}6{\times}1$ for a graphene primitive cell, ZnO $(1{\times}1)$ polar surfaces, and the supercells of the interface. A dipole correction [70] was applied to make the computations converge more quickly and to eliminate the artificial electrostatic field between periodic supercells.

3.1.1 Hubbard U scheme (DFT+U)

Since DFT$-$GGA severely underestimates the band gap of ZnO by giving a wrong energy position of the Zn 3d orbital, we adopted the GGA + U method [37] to partially correct this issue, where the effective on-site Coulomb interaction parameter U and exchange interaction parameter J are 9.5 and 0.0 eV, respectively. Although adopting hybrid functionals, where the Hartree-Fock exchange is partially combined with the DFT exchange would be a more accurate strategy, it would be prohibitively expensive from a computing standpoint because this material has too many orbitals for Hartree-Fock to handle. Traditional density functionals are unable to give a correct description of van der Waals (vdW) interactions because of dynamical correlations between fluctuating charge distributions. In the models of the interface, vdW interactions are expected to be significant and thus the DFT-D2 method of Grimme [71], which is successful for graphene/SiC interface structures [72] was adopted in this work. The total energy (E_{total}) is represented as:

$$E_{total} = E_{KS-DFT} + E_{vdW} \tag{3.1}$$

where E_{KS-DFT} is the conventional Kohn-Sham DFT energy and E_{vdW} is the dispersion correction. Note that Vanin et al [73] reported that the vdW-DF method proposed by Dion et al [74] failed to reproduce the experimental observations of the metal-graphene interface. When doing a spin polarized computation, a magnetic moment on each atom is allowed to relax to its optimum value.

In this work, the ZnO wurtzite structure with unit cells of 6 atoms in $P6_{3mc}$ is taken into consideration. After these frameworks were set up, literature resources [75], were carefully followed. The number of states that are occupied at a given level of energy is used to compute the density of states (DOS). Tetrahedron approach was used to do Brillouin zone integration, and it has been shown to be effective, particularly for calculations of excited states and dielectric functions [76].

3.1.2 Technical Detail of Convergence Test

Plane Wave Basis Sets and K-Point Sampling

The plane wave basis set is used for the expansion of electron wavefunctions, see Eqs. 2.16-2.25. The k-points & cut-off energies chosen would impact on total energy of the system. Our calculations show that k-mesh of $6\times6\times6$ can be optimum in the bulk calculation of this structure as shown in Fig. 3.1. With a fixed k-mesh of $6\times6\times6$, a convergence test of the total energy with respect to energy cut-off is shown in Fig. 3.2. Thus, for the band structure calculation, a cut-off energy of E_{cut} = 400 eV and a k-point

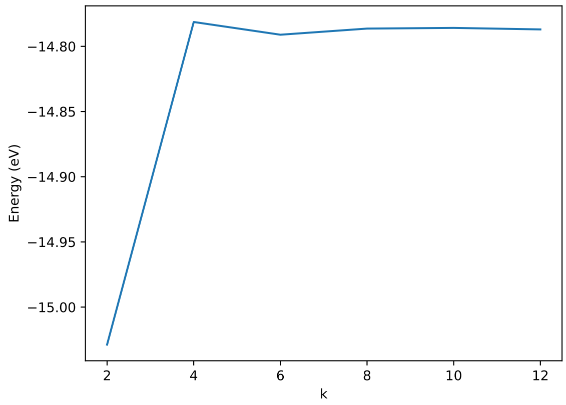

Figure 3.1: Convergence test of the total energy with respect to k-point sampling.

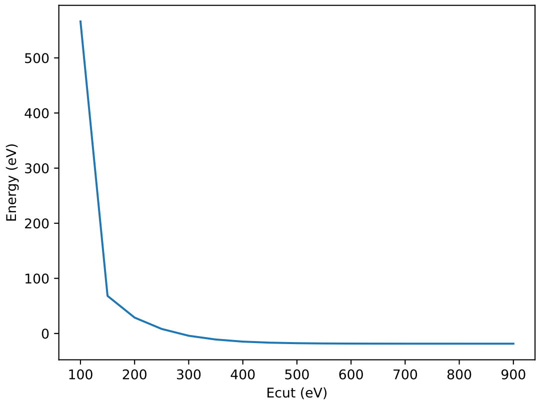

Figure 3.2: Convergence test of the total energy with respect to cut-off energy.

mesh of $6\times6\times6$ points were chosen.

3.1.3 GPAW capabilities

GPAW is a density-functional theory (DFT) based on the projector-augmented wave (PAW) method and the atomic simulation environment (ASE). The wave functions can be described with

- Plane-waves (pw).
- Real-space uniform grids, multigrid methods and the finite-difference approximation (fd).
- Atom-centered basis-functions (lcao).

In this work, the pw basis has been applied.

Projector-augmented wave (PAWs) pseudopotential

The projector augmented wave method (PAW) is a technique used in ab-initio electronic structure calculations. It is a generalization of the pseudopotential and linear augmented-plane-wave methods, and allows for density functional theory calculations to be performed with greater computational efficiency [43, 77].

Chapter 4

Results and Discussion

4.1 Structural, electronic and optical properties of bulk ZnO

4.1.1 Bulk properties of ZnO

Cohesive energy of bulk ZnO

The cohesive energy [eV/atom] is defined as the energy required to dissociate the alloy compound into free (neutral) atoms. It is calculated according to:

$$E_{\mathrm{coh}} = -\frac{1}{\mathrm{N}}\left(\mathrm{E}_{\mathrm{bulk}} - \sum_{\mathrm{atom}} \mathrm{E}_{\mathrm{atom}}\right) \tag{4.1}$$

where E_{coh} is the cohesive energy, N is the number of atoms in the unit cell of the zinc-oxygen alloy. E_{atom} is the atomic energy of a ground state zinc and oxygen atoms. Accordingly, as shown in Table 4.1, the cohesive energy of bulk ZnO structure in WZ (B_4) $>$ ZB (B_3) $>$ RS (B_1). That means ZnO is more stable in wurtzite (B_4) structure. From energy per atom calculation, WZ (B_4) $>$ ZB (B_3) $>$ RS (B_1). Furthermore, the degree of covalency is shown from charge values to be according to WZ (B_4) $>$ ZB (B_3) $>$ RS (B_1). It appears also necessary to analyze prospect of bulk vacancy formations. The vacancy formation energy E_{vac} [eV] is defined as:

$$E_{\mathrm{vac}} = \mathrm{E}_{\mathrm{v}} - \frac{\mathrm{N}-1}{\mathrm{N}}\mathrm{E}_{\mathrm{bulk}} \tag{4.2}$$

E_{bulk} is the energy of an N-atom bulk cell without any vacancy and the E_{v} is the bulk potential energy of the same unit cell with a vacancy in it. The vacancy formation energy is the amount of cohesive energy required to create a vacancy. If this value is negative, it signifies that when a vacancy is formed, energy is released.

Table 4.1: Cohesive energy [eV], formation energy [eV], band gap [eV], bulk modulus [GPa] and lattice constant [Å] of bulk ZnO.

Quantity	Source	Structure		
		WZ (B_4)	ZB (B_3)	RS (B_1)
E_{coh}	This work	2.84	1.10	0.94
	Expt value	1.93 [78]	0.96 [78]	0.93 [78]
E_f	This work	-1.25	2.70	2.86
	Expt value	-3.70 [78]	-	-
Bulk modulus	This work	189.5	131.3	169.9
	Expt value	142.4	-	-
Band gap	This work	3.23	3.18	3.99
	Expt value			-
Lattice const (a)	This work	3.4	4.4	4.1
	Expt value	3.25	-	-
Lattice const (c)	This work	5.14	-	-
	Expt value	5.2	-	-
Energy per atom	This work	-3.32	-1.58	-1.41
	Expt value	-	-	-
$\Delta Q[e]$ on Zn	This work	+0.23	+0.25	+0.41
	Expt value	-	-	-
$\Delta Q[e]$ on O	This work	-0.23	-0.25	-0.41
	Expt value	-	-	-

Formation energy of bulk ZnO

The energy necessary to form the alloy compound from its separate elemental bulk structures is represented by energy formation, E_f [eV/atom], which is given by

$$E_\mathrm{f} = \frac{1}{\mathrm{N}}\mathrm{E}_\mathrm{bulk} - \sum_\mathrm{i} \frac{1}{\mathrm{N}_\mathrm{i}}\mathrm{E}_\mathrm{b}^\mathrm{i} \tag{4.3}$$

where N is number of atoms in the unit cell of the alloy compound, E_bulk is total energy of the bulk alloy compound, E_b^i is total energy of bulk of element i, & N_i is number of atoms in the unit cell of the elemental bulk form. In terms of formation energy in reference to Table 4.1, thus, E_f of bulk ZnO structure in WZ (B_4) $<$ ZB (B_3) $<$ RS (B_1). This means ZnO alloy is more favorable to be formed in wurtzite (B_4) structure. Furthermore, based on the bulk modulus values of ZnO structures presented in Table 4.1, WZ (B_4) $>$ ZB (B_3) $>$ RS (B_1). This means, ZnO alloy is more resistant to extreme pressure conditions in wurtzite structure. Negative values of E_f in Eq. (4.3) means exothermic process while positive values mean endothermic process.

Equation of state (EOS) of bulk wurtzite ZnO

We first determine the equilibrium lattice constant and bulk modulus (material's resistance to external pressure), using the equation of state (EOS) for bulk ZnO structures before we proceed to the results obtained in graphene/ZnO hetrostructures. The EOS is obtained by a curve fits (Murnaghan [79] approach) to an energy versus volume calculation data, which also additionally outputs various other important bulk structural parameters, such as minimum volume and minimum energy. The quality of the fits can be seen in Fig. 4.1. Accordingly, the output parameters of lattice constants (a), (c), and bulk modulus (B) for B_4 structure in this work are 3.4 Å, 5.14 Å, and 137.59 GPa respectively. But the experimental results of lattice constants (a), (c), and bulk modulus (B) are 3.25 Å [80], 5.2 Å [80], and 142.4 GPa [81], respectively. The results presented in Table 4.1 show that even if there is small difference in between the computational and the experimental results, the two are essentially in agreement with each other.

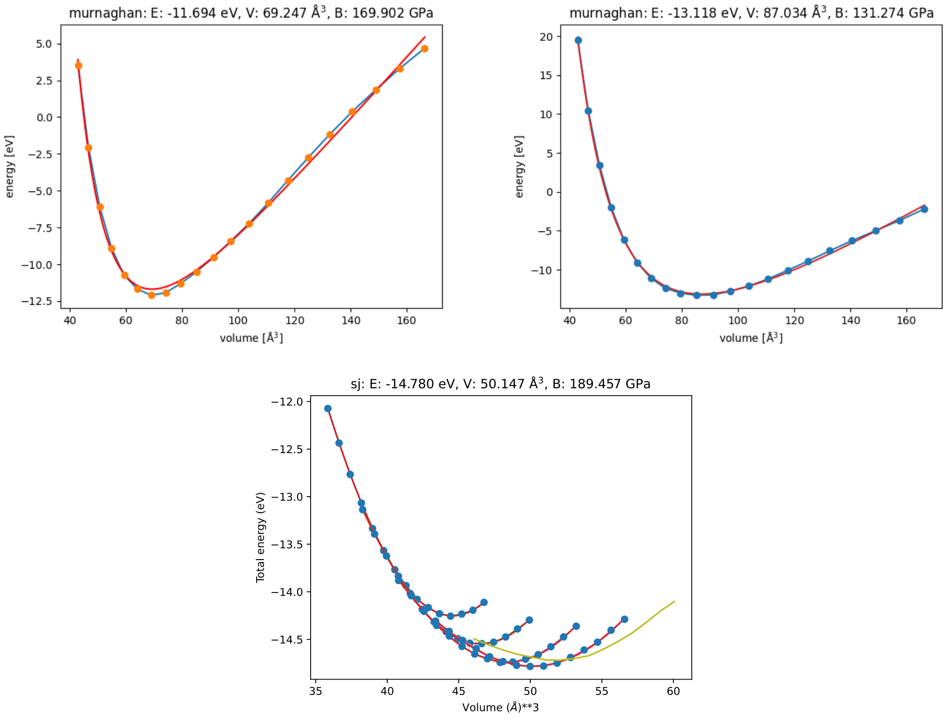

Figure 4.1: Energy versus volume graph of rocksalt, zinc blende, and wurtzite structures (from left to right).

4.1.2 Electronic Properties of bulk wurtzite ZnO

The electronic properties are among the most studied features in ZnO. In general, the energy band structure and density of states (DOS) are computed to represent the electronic behavior of ZnO, which are useful in the device design.

DOS and PDOS of bulk wurtzite ZnO

The DOS and PDOS curves for bulk ZnO in wurtzite structure is presented in Figs. 4.2 & 4.3. The lower part of the valence band at an energy $\sim$ -7 eV to $\sim$ -4 eV shows narrow sharp peaks in DOS, see Fig. 4.2(a)&(b). The projected/partial density of states (PDOS) is the relative contribution of a particular atom/orbital to the DOS. As shown in Fig. 4.3, the p and s orbitals contribute to the occupation states of DOS. The p orbital has most states for occupation followed by s orbital. The p states dominate near the Fermi level, while the s states contributes in the deepest energy level.

Band structure of bulk wurtzite ZnO

From Fig. 4.4, it can be seen that the valence band maxima and conduction band minima lie on the same image point, Γ, indicating direct band. The band structure in the figure for wurtzite bulk ZnO, point $\Gamma - \Gamma$ showed the lowest energy band gap, which is $\sim$ 3.23 eV. The excitation of electrons (from the highest valence band to the lowest conduction band) will occur at the lowest energy band gap. Thus, point $(\Gamma - \Gamma)$ is the point where electron excitation most probably occurred. The computed band gap is in agreement with the experimental value 3.37 eV. ZnO is classed as being between an ionic and covalent compound [82].

Charge and charge density of bulk wurtzite ZnO

Atoms within bulk materials or molecules have a net charge. An elegant method that is applicable within plane-wave calculations is the Bader decomposition, which uses stationary points in the three-dimensional electron density to partition electrons among different atoms. Tables 4.2 shows the DFT outputs of atomic charge form (ACF) of bulk ZnO. Table 4.2 revealing that 2.448 electrons have been transferred from zinc atoms to the oxygen atoms. This shows zinc atom become p-type and oxygen atom n-type material.

Electronic charge distribution of bulk wurtzite ZnO

The electron density contours denotes the charge distribution in an atom, which in turn also establish the nature of the bond among different atoms. In addition, electronic charge density map serves as a complementary tool for achieving a proper understanding

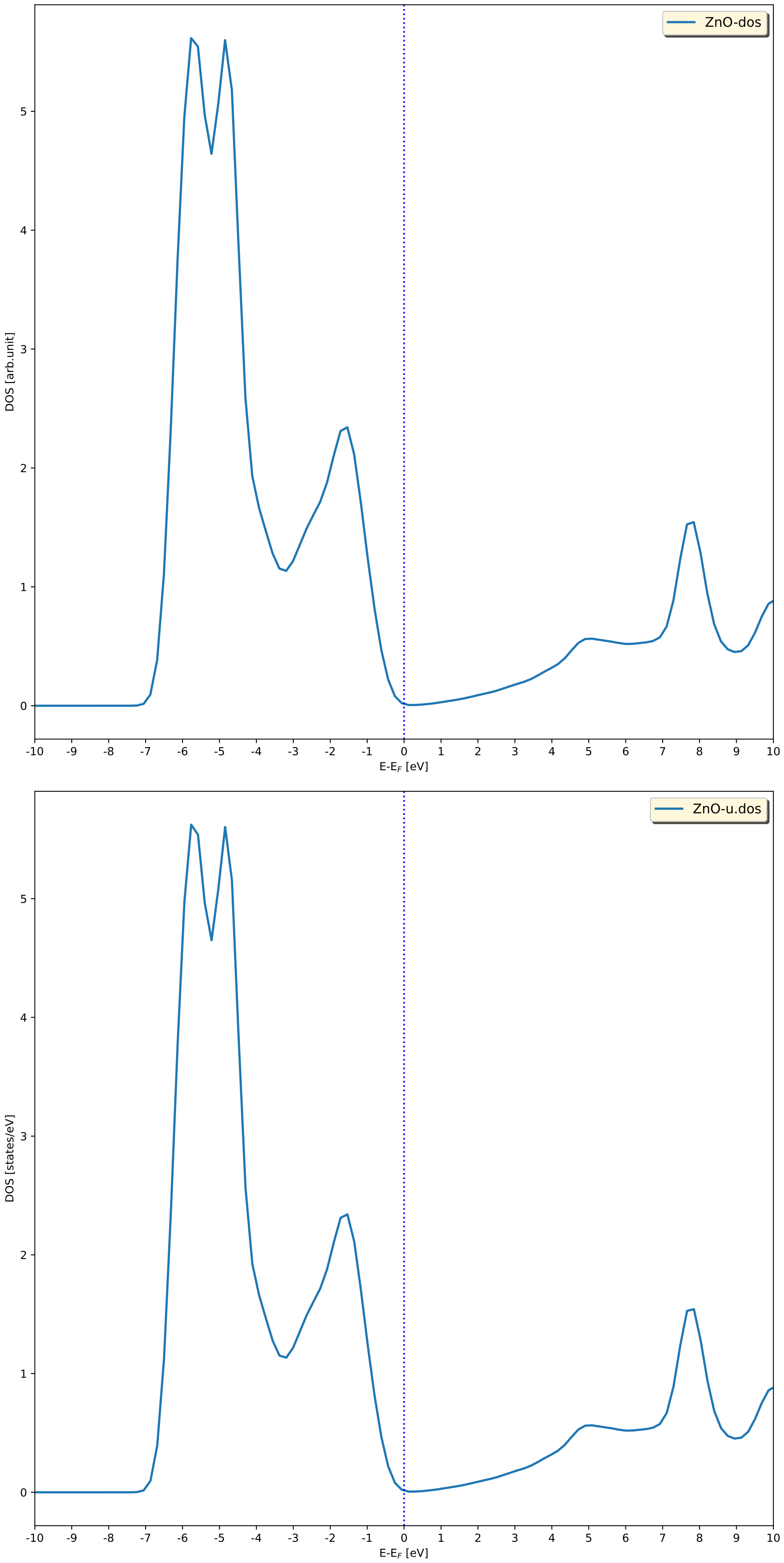

Figure 4.2: DOS for bulk wurtzite ZnO without and with correction.

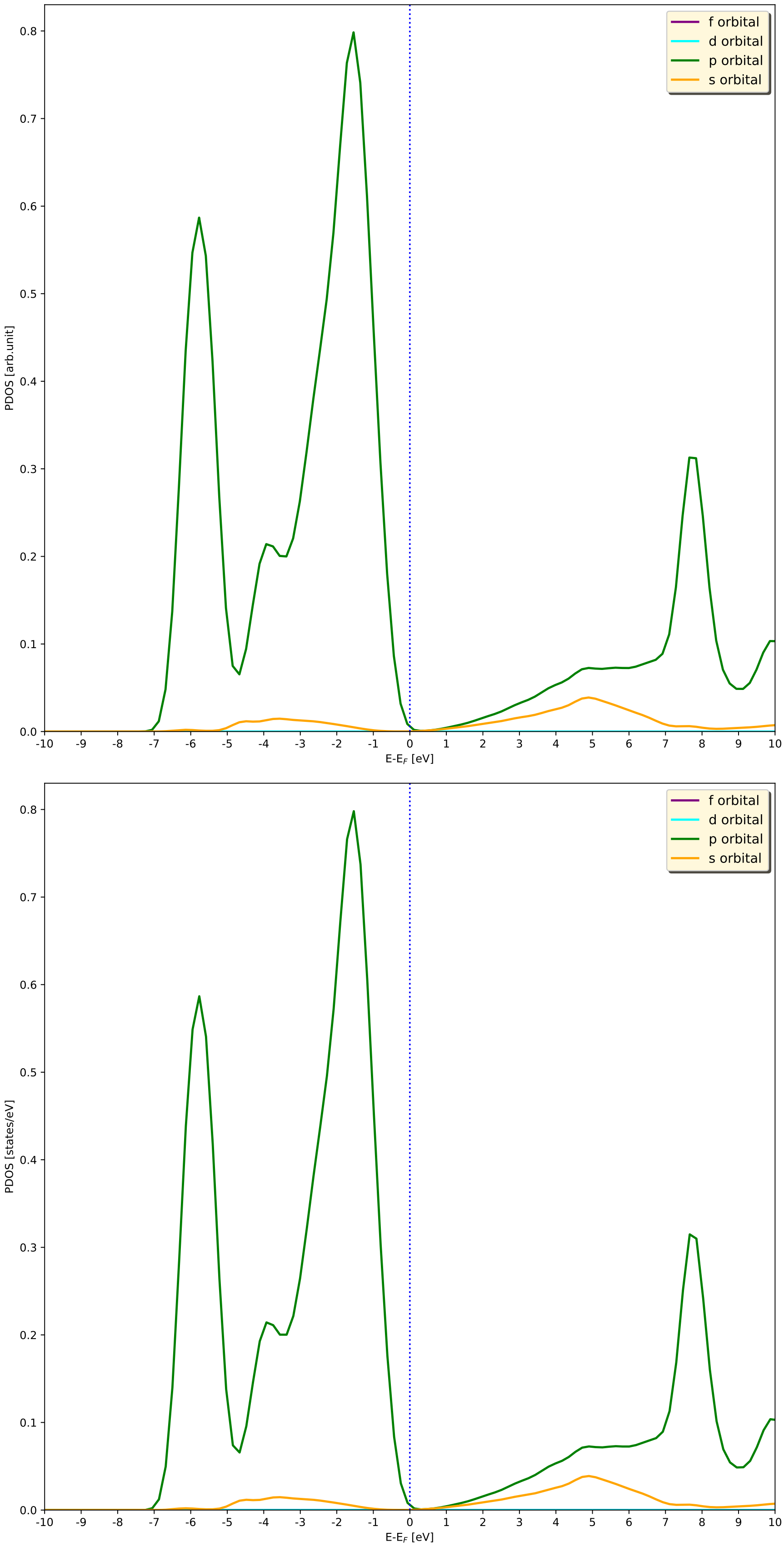

Figure 4.3: PDOS for bulk wurtzite ZnO without and with correction.

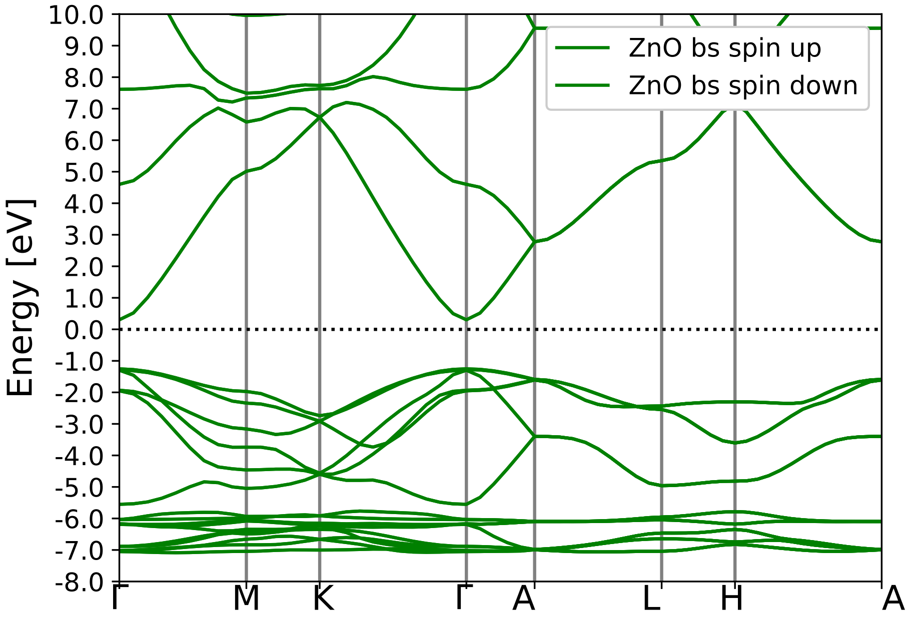

Figure 4.4: Wurtzite bulk ZnO.

Table 4.2: ACF DFT output of wurtzite bulk ZnO.

atom	x	y	z	charge	MIN DIST	ATOMIC VOL
O	0.000000	0.000000	-0.022019	9.223563	1.793307	89.626100
Zn	0.000000	0.000000	3.792645	28.776254	1.665610	79.632197
O	3.118048	1.800206	5.004675	9.224450	1.782926	89.674536
Zn	3.118048	1.800206	8.819317	28.777073	1.661071	79.657383

of the electronic structure of the system being studied, as shown in Fig. 4.5. The ionic and covalent character of material can be related to charge transfer and sharing between the cation and anion.

4.1.3 Optical properties of bulk wurtzite ZnO

The imaginary part, ε_2, of dielectric function measures the energy absorption as a result of charge excitation, whereas the real part, ε_1, measures the strength of dynamical screening and the polarization effects [83]. Hence, a typical plot of imaginary part, ε_2, is sufficient to explain the transition phenomena. As shown in Fig. 4.6, the real and the imaginary parts of complex dielectric function completly describes the optical properties of a medium for different photon energies. The peak value of real (the dispersive part) part of the dielectric constant is related the electron excitation. For the real part, $\varepsilon_1(\omega)$, of the dielectric function in Fig. 4.6 (yellow color line), the highest peak for ZnO appears around 0.59 eV and the $\varepsilon_1(\omega)$ at this photon energy is 25.66. On the other hand, the

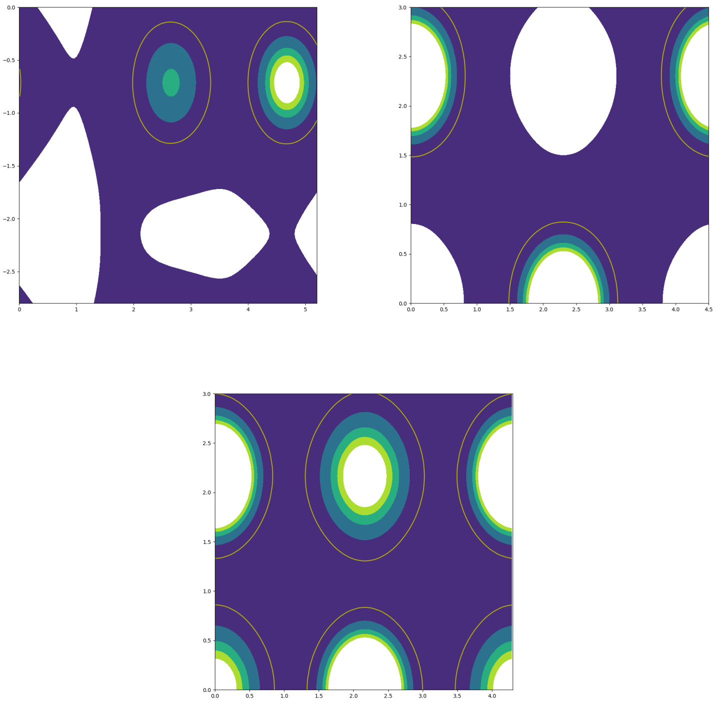

Figure 4.5: Electronic charge density graph of B_4, B_3, and B_1 structures of bulk ZnO (from left to right, respectively).

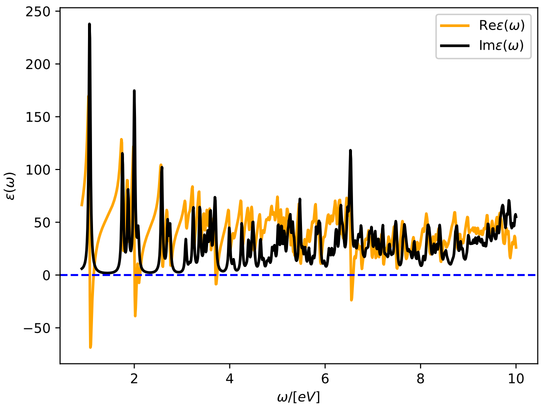

Figure 4.6: The real (yellow color line) and imaginary (black color line) parts of frequency-dependent complex dielectric function of wurtzite bulk ZnO with local field effects.

imaginary part $\varepsilon_2(\omega)$ (absorptive part) of the dielectric function in Fig. 4.6 (black color line) illustrates the optical transition mechanism. Each peak in the imaginary part of the dielectric function corresponds to an electronic transition. The major $\varepsilon_2(\omega)$ peak for ZnO is located at 0.61 eV, and the value of $\varepsilon_2(\omega)$ at this photon energy is 36.69, and corresponds to the transition of electrons from occupied VB to unoccupied CB.

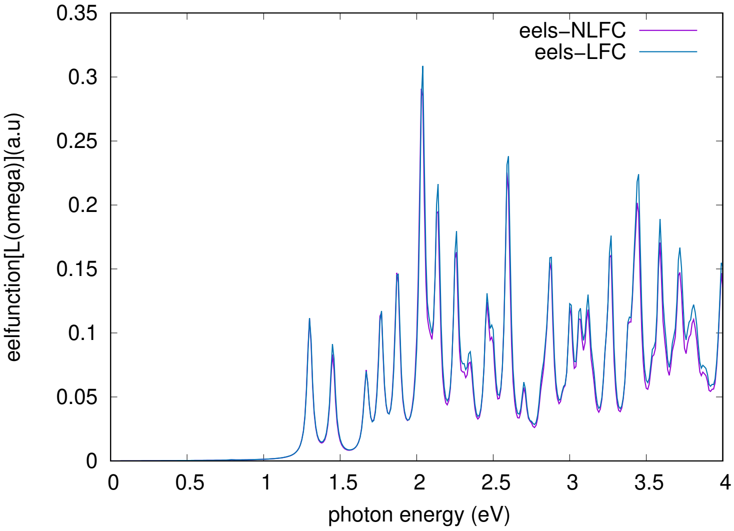

Figure 4.7: Electron energy loss spectrum for bulk wurtzite ZnO.

Electron energy loss spectrum

The EELS function is an important factor that describes the energy loss of a fast electron passing through the material. In this case, we represent the EELS function for an energy interval [0-4] eV. The variation of the EELS function of bulk wurtzite ZnO is shown in the Fig. 4.7 below. The peaks correspond to the plasma resonance and the corresponding frequency is called the plasma frequency ω_p. The resonant energy loss occurs at an energy of about 2.1 eV for all directions.

The absorption coefficient $\alpha(\omega)$

The absorption coefficient depends on the material and also on the wavelength of the light that is absorbed. As can be seen from Fig. 4.8, the absorption coefficient $\alpha(\omega)$ of bulk ZnO increases as the photon energy increases. Peak of absorption coefficient value, $\sim$ 0.031, is reached at a photon energy of $\sim$ 6.9 eV. Absorption will not take place when the photon energy is less than the energy of the optical gap.

Index of refraction $n(\omega)$

The propagation of a light beam through a translucent medium is described by the refractive index n. As shown in Fig. 4.9, the peak value of refractive index of bulk ZnO is around 4 eV. The value of the refractive index decreases as the photon energy, that is incident on the surface of bulk ZnO, increases from 0-6.6 eV, and then increases up to 10 eV.

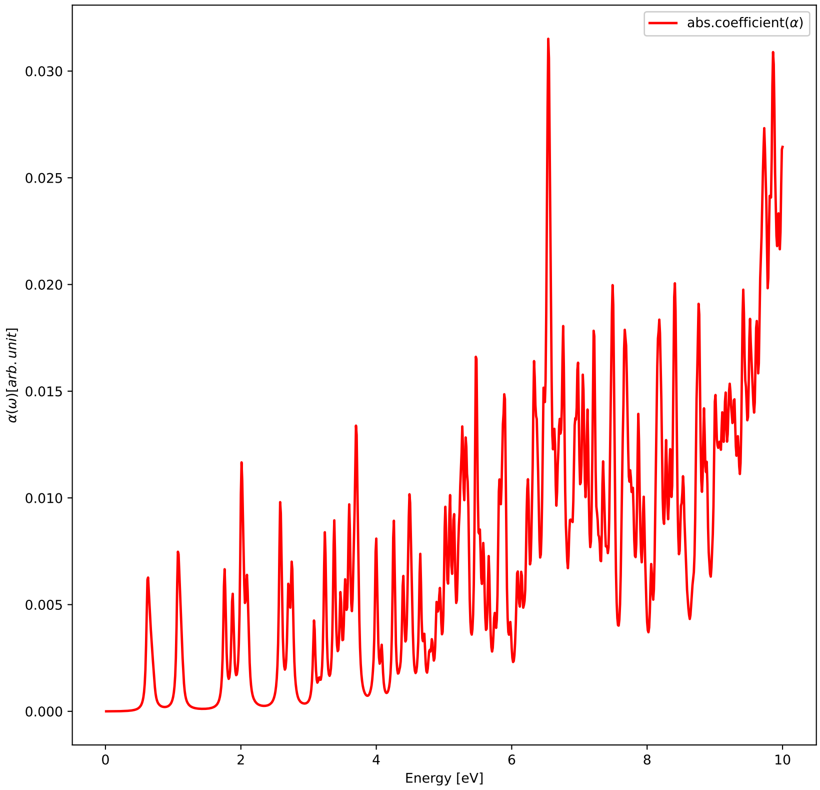

Figure 4.8: Absorption coefficient of bulk wurtzite ZnO as a function of energy.

Reflectivity $R(\omega)$

The reflectivity represents the amount of energy reflected in relation to the incident energy. As can be seen, Fig. 4.9 and 4.10 are inversely related. The static values of the reflection coefficient, $R(0)$, is 0.4.

4.2 Surface properties of clean wurtzite ZnO

4.2.1 Surface energy of clean wurtzite ZnO

Surfaces are technologically important in many fields, including catalysis, interfaces, membranes for gas separations, and semiconductor fabrication. Understanding the geometry and electronic structure of surfaces is important. For example, it has been established that there is often a correlation between the structure of a surface and its catalytic activity. The surface energy, E_{surf}, of a material is the energy per unit area required to create a surface and is associated with the stability of the surfaces. A strong molecule attraction is indicated by a high surface energy, whereas, a weak molecular attraction is indicated by a low surface energy. A high surface energy would also indicate increased reactivity with adsorbates, while low surface energy would indicate increased stability. Surface characteristics are extremely important, especially in catalysis. Generally, the

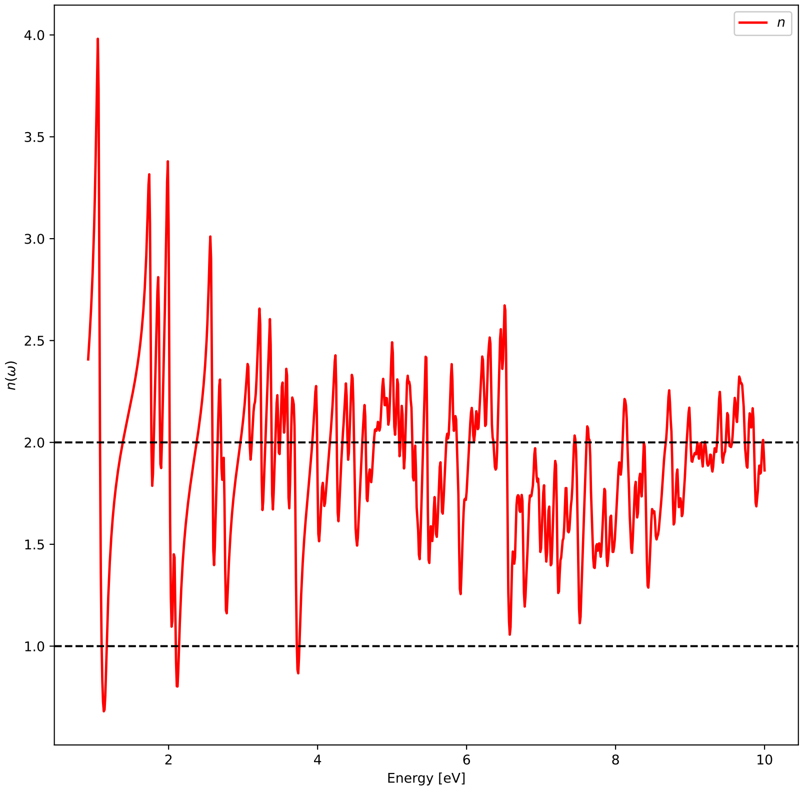

Figure 4.9: Index of refraction of bulk ZnO as a function of energy.

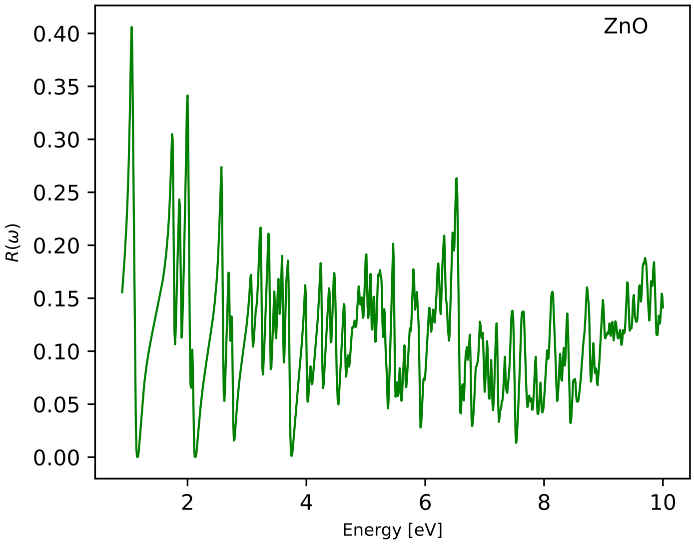

Figure 4.10: The evolution of the reflection coefficient $R(\omega)$ as a function of energy.

surface energy σ [eV/Å^2] is defined as

$$\sigma = \frac{1}{2A}\left(E_{\text{slab}} - \frac{\text{N}_{\text{slab}}}{\text{N}_{\text{bulk}}}\text{E}_{\text{bulk}}\right) \tag{4.4}$$

where E_{slab} denotes the total energy of a slab unit cell, N_{slab}, means number of atoms in the slab unit cell, N_{bulk} means number of atoms in the bulk unit cell, and E_{bulk} is the total energy of a bulk unit cell, A is the surface area of a slab unit cell, and the factor half accounts for the top and bottom surfaces. As shown from Table 4.3, the surface energies for the surface facets increase according to $(001) < (100) < (110) < (111)$ for all the structures. This means (001) surfaces offer a relatively more stable geometries, while (111) facets would likely be expected to be more reactive to impurities / adsorbates. The most stable surfaces of simple materials are typically those with the highest density of surface atoms.

Table 4.3: Surface energy values of wurtzite ZnO surfaces of (001), (100), (110), & (111) facets with their corresponding bulk energy.

Parameter	Surface			
	(001)	(100)	(110)	(111)
Surface energy σ[eV/Å^2]	-21.18	-11.40	-6.61	-6.29
Surface energy [eV]	-443.87	-444.8	-446.05	-444.94

4.2.2 Electronic properties of the clean ZnO surface

DOS and PDOS of clean ZnO surface

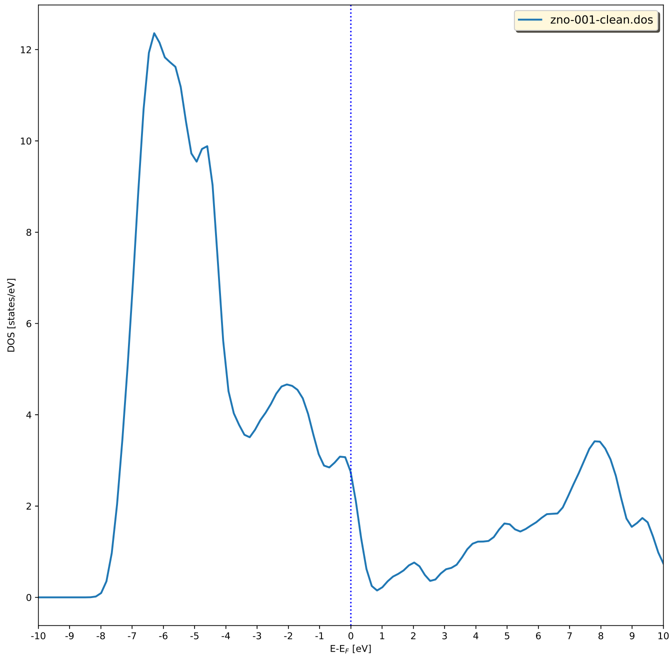

Figure 4.11: DOS of clean ZnO (001).

As shown from Fig. 4.11, the DOS value of the clean surface of ZnO is maximum in between ∼-8 eV to ∼-6.5 eV. The DOS value is nonzero at the Fermi level and no band gap exists. As shown in Fig. 4.12, the p and s orbitals contribute to the occupation states of DOS. The p orbital has most states for occupation followed by s orbital. The p states dominate near the Fermi level (around -1.5 eV to 1 eV), while the s states contributes in the deepest energy level.

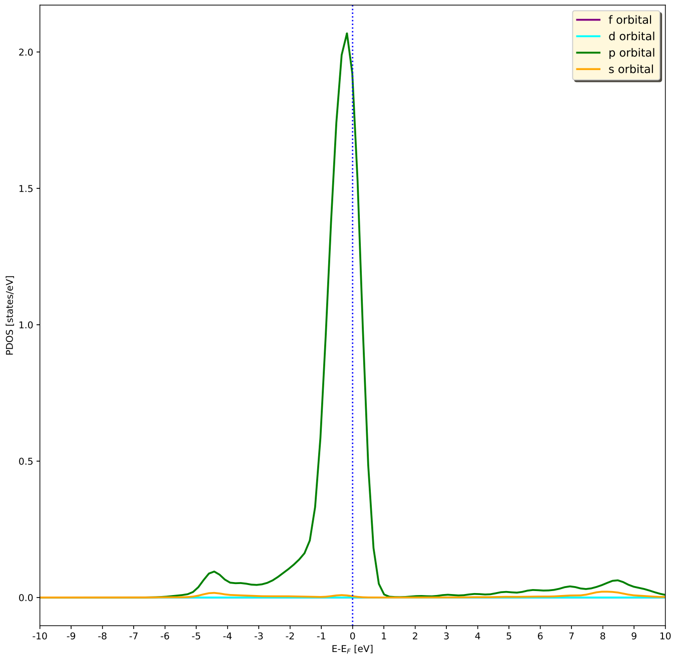

Figure 4.12: PDOS of clean ZnO (001).

4.2.3 Work Function of clean wurtzite ZnO

We used DFT method with GGA-PBE to investigate the workfunction of ZnO and graphene. We investigated the workfunction values on graphene and different ZnO surfaces. We calculated workfunctions of the surfaces in ZnO (0001). This orientation is characterized by two polar surfaces, Zn terminated and O terminated. By surface reconstruction of ZnO polar surfaces (0001) and $(000\bar{1})$ using Miller indices on the surface of ZB (fcc) structure as (001), (100), (110), and (111), the values of the work function on each surfaces is presented in Table 4.4. The experimental work function value of graphene is 4.6 eV [84]. For the clean ZnO (0001)-Zn surface, we obtain a work function value of 4.3 to 6.8 eV, and the literature values for ZnO surfaces vary between 3.7 and 6.0 eV [85]. Even if there is a small difference in between the two results, they are essentially in agreement with each other.

As can be shown in Table 4.4, there is a difference in the calculated work function of graphene and the polar surface of ZnO (001) at the interfaces. The difference in between the work function of graphene and polar surface of ZnO(001), shows the charge transfer

Table 4.4: The calculated work function [eV] of ZnO and graphene with GGA + U correction on different surfaces.

Quantity	Source	Structure			
		(001)	(100)	(110)	(111)
Work function [eV]	This work	6.8	4.48	4.27	4.94
	Expt value	-	-	-	-

between the interfaces. Since the work function of ZnO(001) polar surface is greater than graphene, then ZnO(001) polar surface is able to be doped with graphene.

4.3 Structural and electronic properties of graphene/ZnO heterojunction

4.3.1 Structural properties of graphene/ZnO hetrojunction

We considered the adsorption of graphene on ZnO polar surfaces. The adsorption energy of graphene layer is defined by

$$E_{ads} = E_{interface} - E_{graphene} - E_{ZnO} \tag{4.5}$$

while,

$$e_{ads} = \frac{E_{interface} - E_{graphene} - E_{ZnO}}{n} \tag{4.6}$$

where e_{ads} [eV/atom] is the adsorption energy per C atom; $E_{\text{interface}}$, E_{graphene}, and E_{ZnO} is the total energies of the interface, graphene, and ZnO surface, respectively; n is the total number of carbon atoms in the interface. Figure 4.13 shows that the adsorption behaviors of the three configurations for ZnO(0001) and $(000\bar{1})$ surfaces are almost the same.

More importantly, the long range vdW interaction plays an important role in the adsorption. Both physical and chemical adsorptions take place when graphene adheres to bare SiC [86], SiO_2 [87], and metals [88] surfaces. However, no chemical adsorption is seen when graphene adheres to ZnO surfaces. For use in photocatalysts and solar cells, the intimate but nondestructive contact between graphene and ZnO may be unique. The shortest separation distance between an atom of the adsorbed ZnO and the closest C atom of the graphene monolayer in the graphene/ZnO is 2.52 Å, which is in agreement with a literature result [89]. It looks that some sort of charge transfer from graphene layer to the underlying ZnO surface takes place at such optimum separation distance, while also the corresponding energy per atom and cohesive energies show stabilities of the structure. The geometries of interface structures of the heterojunction is given in

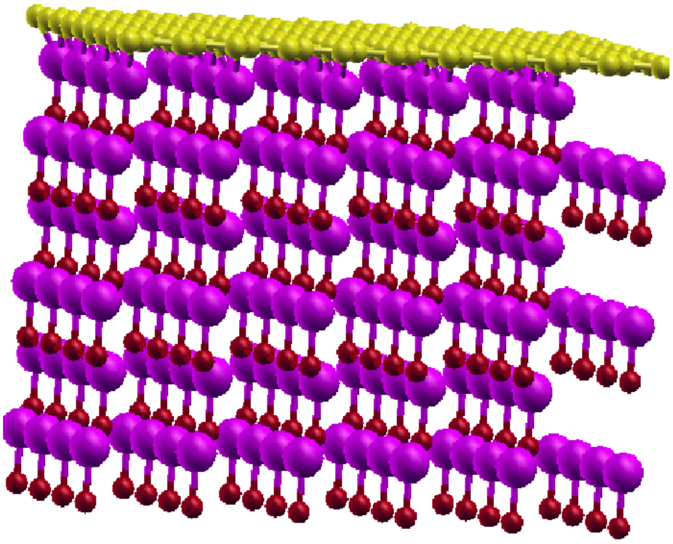

Figure 4.13: Graphene/ZnO heterojunction structure. Color Online. Colors: C-yellow, Zn-pink, O-red.

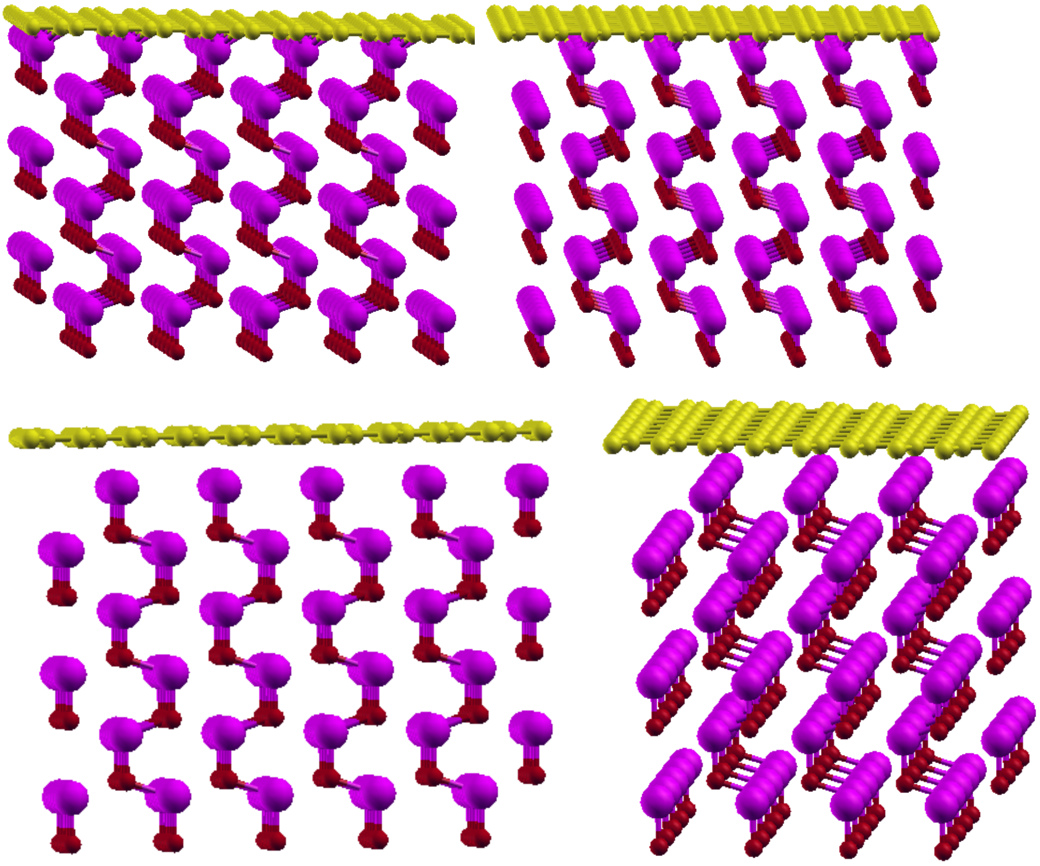

Figure 4.14: ZnO-001-clean-T-graphene at different equlibrium distance. Top to bottom, $d = 1.02$ Å, $d = 1.52$ Å, $d = 2.12$ Å, $d = 2.52$ Å, respectively. Color Online. Colors: C-yellow, Zn-pink, O-red.

Table 4.5: Adsorption energy per atom, cohesive energy, and ΔQ (charge transfer from graphene to the interface) as a function of $\frac{d_0-d}{d_0}$. Color Online. Colors: purple color solid circle for cohesive energy; blue color filled square for charge.

Quantity	$\frac{d_0-d}{d_0}$							
	0.99	0.79	0.59	0.39	0.27	0.00	0.15	-0.19
Energy per atom [eV]	-18.31	-14.19	-9.92	-8.60	-8.43	-8.39	-8.38	-8.36
Cohesive Energy [eV]	1.25	2.9	4.61	5.13	5.21	5.22	5.22	5.23
ΔQ [e]	+0.63	+0.19	-0.38	-0.33	-0.23	-0.13	+0.05	+0.11

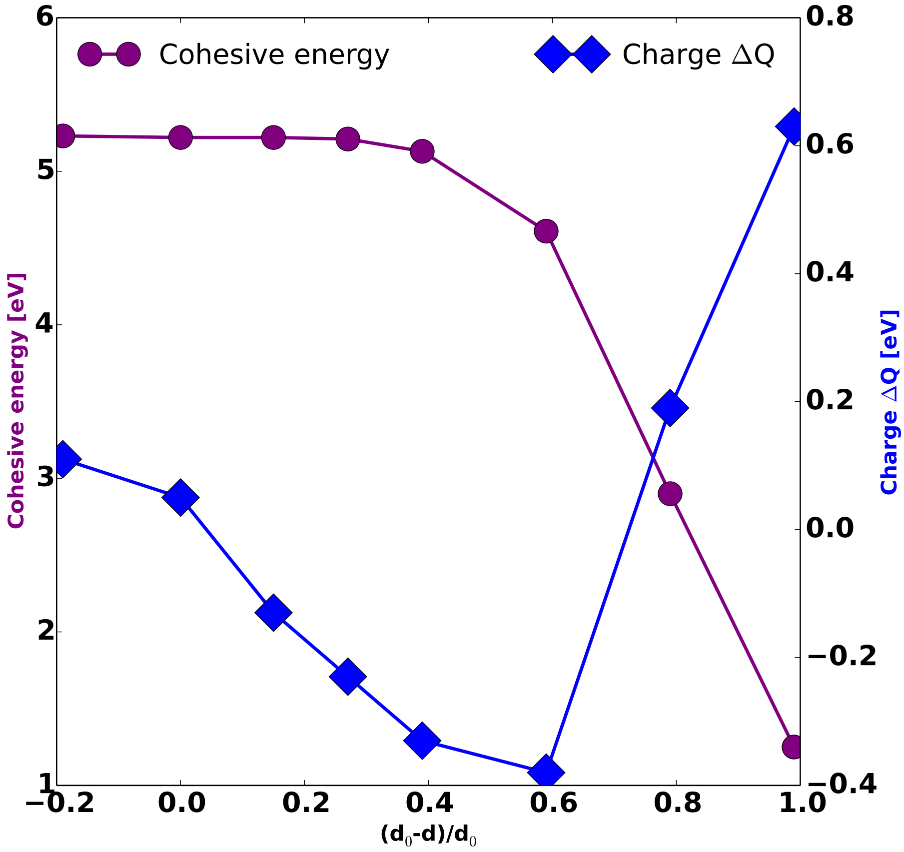

Figure 4.15: Cohesive energy and charge transfer ΔQ as a function of $\frac{d_0-d}{d_0}$. Color Online. Purple color: Cohesive energy, and blue color: ΔQ.

Fig. 4.14, while the corresponding graphic plots of the cohesive and adsorption energies trends are given in Figs. 4.15 & 4.16, respectively. Table 4.5 give quantitative values of the adsorption and cohesive energies.

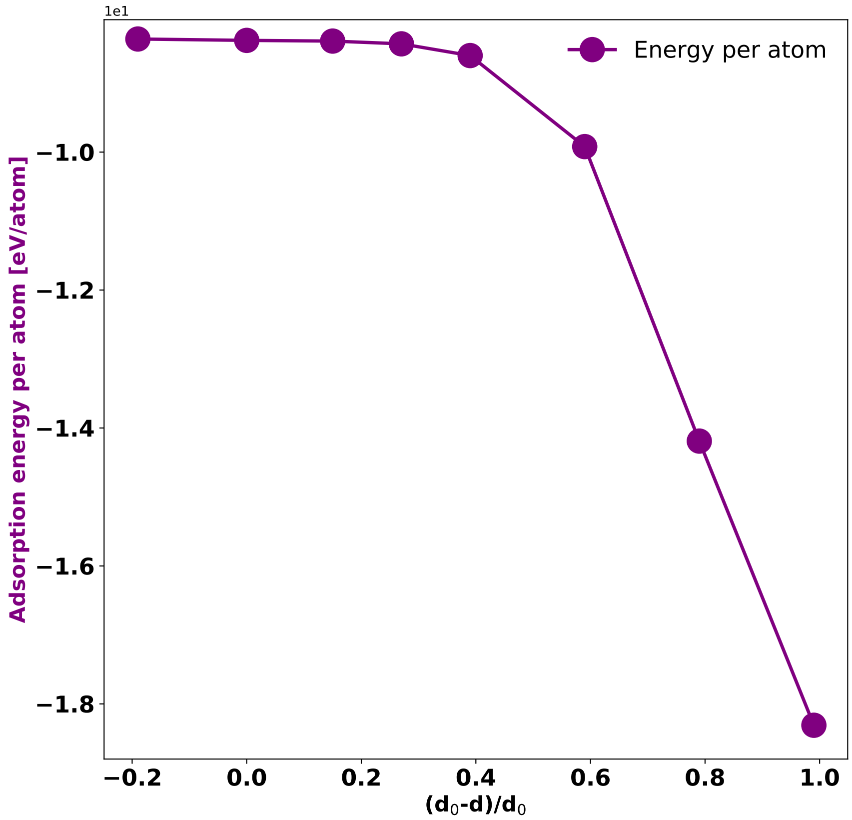

Figure 4.16: Adsorption energy per atom as a function of $\frac{d_0-d}{d_0}$.

4.3.2 Electronic properties of graphene/ZnO heterojunction

DOS for graphene/ZnO heterojunction

As shown in Fig. 4.17, the graphene/ZnO heterojunction shows a narrow sharp peak in the DOS at ∼-8 eV to ∼-4.5 eV which is associated with a large quantity of generated states in the valence band and nonzero DOS at the Fermi energy, indicating that graphene/ZnO has a metalic character.

PDOS of graphene/ZnO heterojunction

As PDOS is the relative contribution of a particular atom/orbital to the DOS, as shown in Fig. 4.18, the p and s orbitals contribute to the occupation states of DOS. The p orbital has a major contribution and the s orbital has a minor contribution to the DOS in both the conduction and valence bands. As shown in Table 4.6, 0.05 electrons have been transferred from graphene atom to the Zinc Oxide. This shows that at the junction, graphene become p-type and ZnO is n-type material. A summary of the charge transfers for different layer separation distances is given in Table 4.5 & Fig. 4.15. While it seems that the heterojunction increases the electrical property, (see Figs. 4.17 & 4.18), it remains to be further verified what impact do such effects have on the optical properties. Figure 4.19 shows the 3D counterpart of the 2D layer interface presentations of

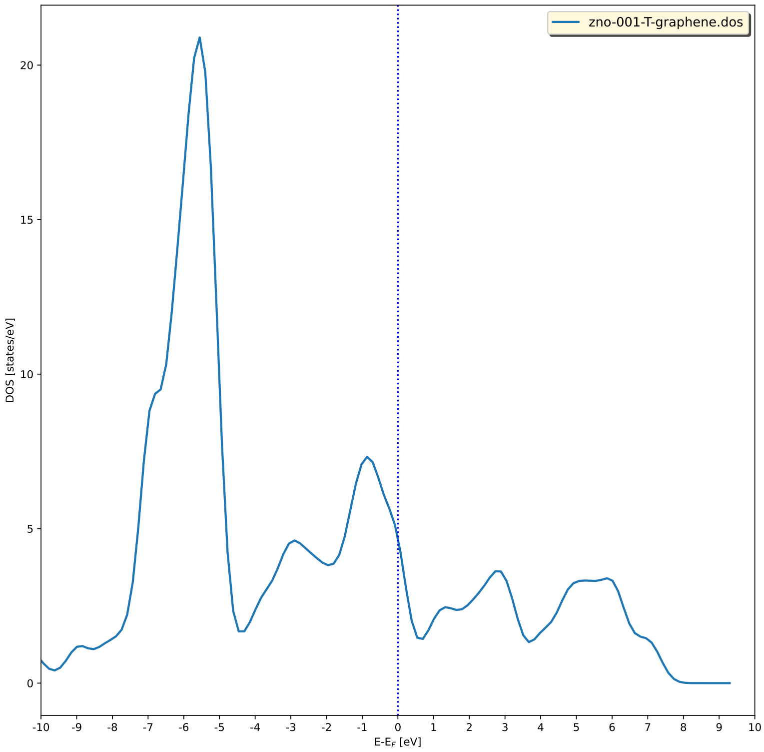

Figure 4.17: DOS of graphene/ZnO heterojunction.

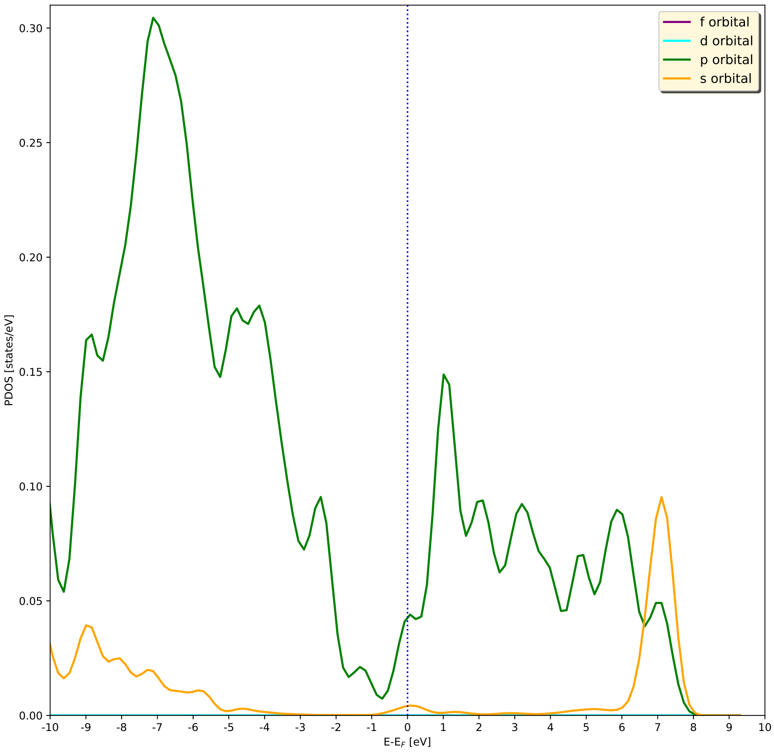

Figure 4.18: PDOS of graphene/ZnO heterojunction.

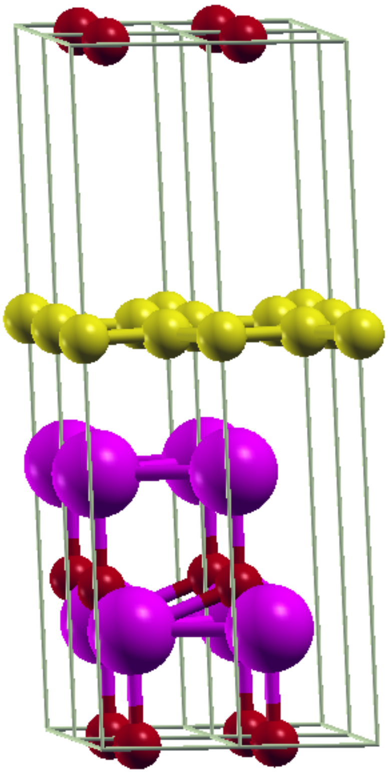

Figure 4.19: 3D view of heterojunction structure. The Corresponding charge calculation is given in Table 4.6. Color Online. Colors: C-yellow, Zn-pink, and O-red.

Table 4.6: Charge calculation output of graphene/ZnO heterojunction.

atom	x	y	z	charge	MIN DIST	ATOMIC VOL
C	0.232573	-0.078379	24.974008	5.863199	1.185250	101.683473
C	2.569241	1.267469	24.973982	6.094329	1.187775	109.959239
O	3.095713	5.359861	8.022798	8.263996	1.695413	168.785384
Zn	3.420928	5.683199	11.475598	29.212156	1.659611	58.948476
O	5.743529	7.010239	14.018855	8.640630	1.750181	58.016523
Zn	5.671568	6.962197	17.912892	29.924967	1.930877	108.737901

VACUUM CHARGE: 0.0000
VACUUM VOLUME: 0.0000
NUMBER OF ELECTRONS: 87.9993

Fig. 4.14. It looks from Figs. 4.15 & 4.16 that the cohesive energies and adsorption energies per atom show saturated values beginning from optimum separation distance of $d_0 = 2.52$ Å.

Chapter 5

Conclusion and Recommendation

5.1 Conclusion

We performed a first principle study of the graphene/ZnO interface. These investigations have been carried out using the Density Functional Theory in the GGA-PBE approximations with Hubbard correction (U) and van der Waals correction. The calculation of the bulk structural, electronic and optical properties of graphene and ZnO reveals various characterstics. The structure, including equilibrium lattice constants, bulk modulus, cohesive, and formation energies are in good agreement with other experimental results. The electronic properties including band gap and band structures, DOS, and PDOS, electronic charge, and charge densities are in a good agreement with the experimental results. The optical properties including the absorption coefficient, the optical conductivity, the refractive index, the reflection coefficient, and the extniction coefficients have revealed interesting characterstics of the system. Surface properties of clean wurtzite ZnO polar surfaces were analysed by calculating the surface energy and work functions.

The surface energies for the surface facets increase according to $(001) < (100) < (110) < (111)$ for all the structures. Based on the outcomes, we suggest that (001) surfaces offer a relatively more stable geometries, while (111) facets would likely be expected to be more reactive to impurities/adsorbates. As a result, we have chosen the polar (001) surface to be suitable for forming the graphene/ZnO heterostructure. The electronic properties of graphene/ZnO heterostructure is revealed in bader charge, DOS, and PDOS analysis. The results show that there is a charge transfer in between graphene and ZnO and the combination/junction seems to show zero band gap. Furthermore, our findings seem to offer compelling justifications for the enhanced photocatalytic efficiency of graphene/ZnO hybrid materials.

5.2 Recommendation for future works

A continual close analysis of the impact of vdW forces between graphene and ZnO, and the allowing for a quick passage of photosensitized electrons between ZnO and graphene requires immediate attention. Whether the intact Dirac point of graphene at the K point indicates a possibility of being a superior electrical conductivity needs to be verified. Further additional studies can also be conducted by increasing the number of adsorbed graphene layers to two and three, and thereby investigate whether doing this results to a reduction or an increase in the possibility of electron-hole recombination.

Bibliography

[1] M. Cinchetti, V. A. Dediu, L. E. Hueso, Activating the molecular spinterface, Nature Materials 16 (2017) 507–515.
URL `https://doi.org/10.1038/nmat4902`

[2] J. Varignon, L. Vila, A. Barthélémy, M. Bibes, A new spin for oxide interfaces, Nature Physics 14 (2018) 322–325.
URL `https://doi.org/10.1038/s41567-018-0112-1`

[3] S. Roche, J. Åkerman, B. Beschoten, J.-C. Charlier, M. Chshiev, S. P. Dash, B. Dlubak, J. Fabian, A. Fert, M. Guimarães, et al., Graphene spintronics: the European Flagship perspective, 2D Materials 2 (2015) 030202.
URL `https://dx.doi.org/10.1088/2053-1583/2/3/030202`

[4] K. S. Novoselov, A. K. Geim, S. V. Morozov, D.-e. Jiang, Y. Zhang, S. V. Dubonos, I. V. Grigorieva, A. A. Firsov, Electric field effect in atomically thin carbon films, Science 306 (2004) 666–669.
URL `https://www.science.org/doi/abs/10.1126/science.1102896`

[5] S. Morozov, K. Novoselov, M. Katsnelson, F. Schedin, D. C. Elias, J. A. Jaszczak, A. Geim, Giant intrinsic carrier mobilities in graphene and its bilayer, Physical Review Letters 100 (2008) 016602.
URL `https://doi.org/10.1103/PhysRevLett.100.016602`

[6] X. Ding, H. Sun, X. Xie, H. Ren, F. Huang, M. Jiang, Anomalous paramagnetism in graphene on hexagonal boron nitride substrates, Physical Review B 84 (2011) 174417.
URL `https://doi.org/10.1103/PhysRevB.84.174417`

[7] A. Mattausch, O. Pankratov, Ab initio study of graphene on SiC, Physical Review Letters 99 (2007) 076802.
URL `https://doi.org/10.1103/PhysRevLett.99.076802`

[8] S. Bleikamp, P. J. Feibelman, T. Michely, et al., Two-dimensional Ir cluster lattice on a graphene moiré on Ir (111), Physical Review Letters 97 (2006) 215501.
URL `https://doi.org/10.1103/PhysRevLett.97.215501`

[9] M. Z. Hossain, Chemistry at the graphene-sio$_2$ interface, Applied Physics Letters 95 (2009) 143125.
URL `https://doi.org/10.1063/1.3247964`

[10] X. Li, W. Cai, J. An, S. Kim, J. Nah, D. Yang, R. Piner, A. Velamakanni, I. Jung, E. Tutuc, et al., Large-area synthesis of high-quality and uniform graphene films on copper foils, Science 324 (2009) 1312–1314.
URL `https://www.science.org/doi/10.1126/science.1171245`

[11] A. Venugopal, L. Colombo, E. Vogel, Contact resistance in few and multilayer graphene devices, Applied Physics Letters 96 (2010) 013512.
URL `https://doi.org/10.1063/1.3290248`

[12] B. Huard, N. Stander, J. Sulpizio, D. Goldhaber-Gordon, Evidence of the role of contacts on the observed electron-hole asymmetry in graphene, Physical Review B 78 (2008) 121402.
URL `https://doi.org/10.1103/PhysRevB.78.121402`

[13] Ü. Özgür, Y. I. Alivov, C. Liu, A. Teke, M. Reshchikov, S. Doğan, V. Avrutin, S.-J. Cho, Morkoç, H, A comprehensive review of ZnO materials and devices, Journal of Applied Physics 98 (2005) 11.
URL `https://doi.org/10.1063/1.1992666`

[14] J. Zhou, N. S. Xu, Z. L. Wang, Dissolving behavior and stability of ZnO wires in biofluids: a study on biodegradability and biocompatibility of ZnO nanostructures, Advanced Materials 18 (2006) 2432–2435.
URL `https://doi.org/10.1002/adma.200600200`

[15] Z. Zhou, T. Komori, M. Yoshino, M. Morinaga, N. Matsunami, A. Koizumi, Y. Takeda, Enhanced 1.54 μ m photoluminescence from Er-containing ZnO through nitrogen doping, Applied Physics Letters 86 (2005) 041107.
URL `https://doi.org/10.1063/1.1856692`

[16] Z. Yin, S. Wu, X. Zhou, X. Huang, Q. Zhang, F. Boey, H. Zhang, Electrochemical deposition of ZnO nanorods on transparent reduced graphene oxide electrodes for hybrid solar cells, Small 6 (2010) 307–312.
URL `https://doi.org/10.1002/smll.200901968`

[17] T. Kavitha, A. I. Gopalan, K.-P. Lee, S.-Y. Park, Glucose sensing, photocatalytic and antibacterial properties of graphene–ZnO nanoparticle hybrids, Carbon 50 (2012) 2994–3000.
URL `https://doi.org/10.1016/j.carbon.2012.02.082`

[18] W. Geng, X. Zhao, H. Liu, X. Yao, Influence of interface structure on the properties of ZnO/graphene composites: a theoretical study by density functional theory calculations, The Journal of Physical Chemistry C 117 (2013) 10536–10544.
URL `https://doi.org/10.1021/jp401733h`

[19] P. Hohenberg, W. Kohn, Inhomogeneous electron gas, Physical Review 136 (1964) B864.
URL `https://doi.org/10.1103/PhysRev.136.B864`

[20] W. Kohn, L. J. Sham, Self-consistent equations including exchange and correlation effects, Physical Review 140 (4A) (1965) A1133.
URL `https://doi.org/10.1103/PhysRev.140.A1133`

[21] W. Schiehlen (Ed.), Multibody systems handbook, Springer-Verlag, Berlin, Heidelberg, 1990.
URL `https://doi.org/10.1007/978-3-642-50995-7`

[22] L. Tian, Density Functional Theory study of bulk properties of metallic alloys and compounds, Ph.D. thesis, KTH Royal Institute of Technology (2017).

[23] M. D. Segall, P. J. D. Lindan, M. J. Probert, C. J. Pickard, P. J. Hasnip, S. J. Clark, M. C. Payne, First-principles simulation: ideas, illustrations and the CASTEP code, Journal of Physics: Condensed Matter 14 (2002) 2717.
URL `https://dx.doi.org/10.1088/0953-8984/14/11/301`

[24] P. J. Hasnip, K. Refson, M. I. Probert, J. R. Yates, S. J. Clark, C. J. Pickard, Density functional theory in the solid state, Philosophical Transactions of the Royal Society A: Mathematical, Physical and Engineering Sciences 372 (2014) 20130270.
URL `https://doi.org/10.1098/rsta.2013.0270`

[25] M. Stone, Born-Oppenheimer approximation and the origin of Wess-Zumino terms: Some quantum-mechanical examples, Physical Review D 33 (1986) 1191.
URL `https://doi.org/10.1103/PhysRevD.33.1191`

[26] S. Holthaus, Molecular Dynamics Simulation of ZnO, Ph.D. thesis, University of Bremen (2014).

[27] F. Oba, M. Choi, A. Togo, I. Tanaka, Point defects in ZnO: an approach from first principles, Science and Technology of Advanced Materials 12 (2011) 034302.
URL `https://doi.org/10.1088/1468-6996/12/3/034302`

[28] A. B. Kuzmenko, E. Van Heumen, F. Carbone, D. Van Der Marel, Universal optical conductance of graphite, Physical Review Letters 100 (2008) 117401.
URL `https://doi.org/10.1103/PhysRevLett.100.117401`

[29] R. R. Nair, P. Blake, A. N. Grigorenko, K. S. Novoselov, T. J. Booth, T. Stauber, N. M. Peres, A. K. Geim, Fine structure constant defines visual transparency of graphene, Science 320 (2008) 1308–1308.
URL `https://www.science.org/doi/10.1126/science.1156965`

[30] S. Eigler, A new parameter based on graphene for characterizing transparent, conductive materials, Carbon 47 (2009) 2936–2939.
URL `https://doi.org/10.1016/j.carbon.2009.06.047`

[31] Z. Ni, H. Wang, J. Kasim, H. Fan, T. Yu, Y. H. Wu, Y. Feng, Z. Shen, Graphene thickness determination using reflection and contrast spectroscopy, Nano Letters 7 (2007) 2758–2763.
URL `https://doi.org/10.1021/nl071254m`

[32] J. P. Perdew, A. Zunger, Self-interaction correction to density-functional approximations for many-electron systems, Physical Review B 23 (1981) 5048.
URL `https://doi.org/10.1103/PhysRevB.23.5048`

[33] B. Partoens, F. Peeters, From graphene to graphite: Electronic structure around the K point, Physical Review B 74 (2006) 075404.
URL `https://doi.org/10.1103/PhysRevB.74.075404`

[34] C. Xia, F. Wang, C. Hu, Theoretical and experimental studies on electronic structure and optical properties of Cu-doped ZnO, Journal of Alloys and Compounds 589 (2014) 604–608.
URL `https://doi.org/10.1016/j.jallcom.2013.11.066`

[35] J. P. Perdew, K. Burke, M. Ernzerhof, Generalized gradient approximation made simple, Physical Review Letters 77 (1996) 3865.
URL `https://doi.org/10.1103/PhysRevLett.77.3865`

[36] S. J. Clark, M. D. Segall, C. J. Pickard, P. J. Hasnip, M. I. Probert, K. Refson, M. C. Payne, First principles methods using CASTEP, Zeitschrift für kristallographie-crystalline materials 220 (2005) 567–570.
URL `https://doi.org/10.1524/zkri.220.5.567.65075`

[37] B. Himmetoglu, A. Floris, S. De Gironcoli, M. Cococcioni, Hubbard-corrected DFT energy functionals: The LDA+ U description of correlated systems, International Journal of Quantum Chemistry 114 (2014) 14–49.
URL `https://doi.org/10.1002/qua.24521`

[38] V. I. Anisimov, J. Zaanen, O. K. Andersen, Band theory and Mott insulators: Hubbard U instead of Stoner I, Physical Review B 44 (1991) 943.
URL `https://doi.org/10.1103/PhysRevB.44.943`

[39] X.-Y. Deng, G.-H. Liu, X.-P. Jing, G.-S. Tian, On-site correlation of p-electron in d10 semiconductor zinc oxide, International Journal of Quantum Chemistry 114 (2014) 468–472.
URL `https://doi.org/10.1002/qua.24593`

[40] F. Bloch, Quantum mechanics of electrons in crystal lattices, Z. Phys 52 (1928) 555–600.
URL `https://doi.org/10.1098/rspa.1931.0019`

[41] J. C. Phillips, L. Kleinman, New method for calculating wave functions in crystals and molecules, Physical Review 116 (1959) 287.
URL `https://doi.org/10.1103/PhysRev.116.287`

[42] Wikipedia, Pseudopotential - Wikipedia, the free encyclopedia, [Online; accessed 15-May-2021] (2021).
URL `http://en.wikipedia.org/w/index.phptitle=Pseudopotential$&$oldid=1021773745`

[43] P. E. Blöchl, Projector augmented-wave method, Physical Review B 50 (1994) 17953.
URL `https://doi.org/10.1103/PhysRevB.50.17953`

[44] R. M. Martin, Electronic Structure: Basic Theory and Practical Methods, Cambridge University Press, 2004.
URL `https://doi.org/10.1017/CBO9780511805769`

[45] O. Jepson, O. Anderson, The electronic structure of hcp Ytterbium, Solid State Communications 9 (1971) 1763–1767.
URL `https://doi.org/10.1016/0038-1098(71)90313-9`

[46] P. E. Blöchl, O. Jepsen, O. K. Andersen, Improved tetrahedron method for Brillouin-zone integrations, Physical Review B 49 (1994) 16223.
URL `https://doi.org/10.1103/PhysRevB.49.16223`

[47] M. Methfessel, A. Paxton, High-precision sampling for Brillouin-zone integration in metals, Physical Review B 40 (1989) 3616.
URL https://doi.org/10.1103/PhysRevB.40.3616

[48] E. Stolyarova, K. T. Rim, S. Ryu, J. Maultzsch, P. Kim, L. E. Brus, T. F. Heinz, M. S. Hybertsen, G. W. Flynn, High-resolution scanning tunneling microscopy imaging of mesoscopic graphene sheets on an insulating surface, Proceedings of the National Academy of Sciences 104 (2007) 9209–9212.
URL https://doi.org/10.1073/pnas.0703337104

[49] J. C. Meyer, A. K. Geim, M. I. Katsnelson, K. S. Novoselov, T. J. Booth, S. Roth, The structure of suspended graphene sheets, Nature 446 (2007) 60–63.
URL https://doi.org/10.1038/nature05545

[50] J. M. Carlsson, Buckle or break, Nature Materials 6 (2007) 801–802.
URL https://doi.org/10.1038/nmat2051

[51] A. K. Geim, P. Kim, Carbon wonderland, Scientific American 298 (2008) 90–97.
URL http://dx.doi.org/10.1038/scientificamerican0408-90

[52] A. K. Geim, K. S. Novoselov, The rise of graphene, Nature Materials 6 (2007) 183–191.
URL https://doi.org/10.1038/nmat1849

[53] M. Wilson, Electrons in atomically thin carbon sheets behave like massless particles, Physics Today 59 (2006) 21.
URL https://doi.org/10.1063/1.2180163

[54] K. S. Novoselov, A. K. Geim, S. V. Morozov, D. Jiang, M. I. Katsnelson, I. V. Grigorieva, S. Dubonos, a. Firsov, Two-dimensional gas of massless dirac fermions in graphene, Nature 438 (2005) 197–200.
URL https://doi.org/10.1038/nature04233

[55] L. E. Greene, M. Law, D. H. Tan, M. Montano, J. Goldberger, G. Somorjai, P. Yang, General route to vertical ZnO nanowire arrays using textured ZnO seeds, Nano Letters 5 (2005) 1231–1236.
URL https://doi.org/10.1021/nl050788p

[56] F. Oba, M. Choi, A. Togo, I. Tanaka, Point defects in ZnO: an approach from first principles, Science and Technology of Advanced Materials 12 (2011) 034302.
URL https://doi.org/10.1088/1468-6996/12/3/034302

[57] J. D. Patterson, B. C. Bailey, Solid-state physics: introduction to the theory, Springer Science & Business Media, Berlin Heidelberg, 2007.

[58] D. Wickramaratne, F. Zahid, R. K. Lake, Electronic and thermoelectric properties of van der Waals materials with ring-shaped valence bands, Journal of Applied Physics 118 (2015) 075101.
URL https://doi.org/10.1063/1.2838178

[59] X. Ma, B. Lu, D. Li, R. Shi, C. Pan, Y. Zhu, Origin of photocatalytic activation of silver orthophosphate from first-principles, The Journal of Physical Chemistry C 115 (2011) 4680–4687.
URL https://doi.org/10.1021/jp111167u

[60] C. Tang, M. J. Spencer, A. S. Barnard, Activity of ZnO polar surfaces: an insight from surface energies, Physical Chemistry Chemical Physics 16 (2014) 22139–22144.
URL https://doi.org/10.1039/C4CP03221G

[61] C. E. Dreyer, A. Janotti, C. G. Van de Walle, Absolute surface energies of polar and nonpolar planes of GaN, Physical Review B 89 (2014) 081305.
URL https://doi.org/10.1103/PhysRevB.89.081305

[62] N. Lang, W. Kohn, Theory of metal surfaces: work function, Physical Review B 3 (1971) 1215.
URL https://doi.org/10.1103/PhysRevB.3.1215

[63] P. J. Feibelman, D. Hamann, Quantum-size effects in work functions of free-standing and adsorbed thin metal films, Physical Review B 29 (1984) 6463.
URL https://doi.org/10.1103/PhysRevB.29.6463

[64] S. Ciraci, I. P. Batra, Theory of the quantum size effect in simple metals, Physical Review B 33 (1986) 4294.
URL https://doi.org/10.1103/PhysRevB.33.4294

[65] C. Fall, N. Binggeli, A. Baldereschi, Deriving accurate work functions from thin-slab calculations, Journal of Physics: Condensed Matter 11 (1999) 2689.
URL https://dx.doi.org/10.1088/0953-8984/11/13/006

[66] R. Dovesi, B. Civalleri, C. Roetti, V. R. Saunders, R. Orlando, Ab initio quantum simulation in solid state chemistry, Reviews in Computational Chemistry 21 (2005) 1–125.
URL https://doi.org/10.1002/0471720895.ch1

[67] D.-K. Seo, Density functional perturbational orbital theory of spin polarization in electronic systems. I. Formalism, The Journal of Chemical Physics 125 (2006) 154105.
URL https://doi.org/10.1063/1.2354497

[68] J. Enkovaara, C. Rostgaard, J. J. Mortensen, J. Chen, M. Dułak, L. Ferrighi, J. Gavnholt, C. Glinsvad, V. Haikola, H. Hansen, et al., Electronic structure calculations with GPAW: a real-space implementation of the projector augmented-wave method, Journal of Physics: Condensed matter 22 (2010) 253202.
URL `https://dx.doi.org/10.1088/0953-8984/22/25/253202`

[69] H. J. Monkhorst, J. D. Pack, Special points for Brillouin-zone integrations, Physical Review B 13 (1976) 5188.
URL `https://doi.org/10.1103/PhysRevB.13.5188`

[70] G. Makov, M. Payne, Periodic boundary conditions in ab initio calculations, Physical Review B 51 (1995) 4014.
URL `https://doi.org/10.1103/PhysRevB.51.4014`

[71] S. Grimme, Semiempirical GGA-type density functional constructed with a long-range dispersion correction, Journal of Computational Chemistry 27 (2006) 1787–1799.
URL `https://doi.org/10.1002/jcc.20495`

[72] T. Jayasekera, S. Xu, K. W. Kim, M. B. Nardelli, Electronic properties of the graphene/6H-SiC $(000\bar{1})$ interface: A first-principles study, Physical Review B 84 (2011) 035442.
URL `https://doi.org/10.1103/PhysRevB.84.035442`

[73] M. Vanin, J. J. Mortensen, A. Kelkkanen, J. M. Garcia-Lastra, K. S. Thygesen, K. W. Jacobsen, Graphene on metals: A van der Waals density functional study, Physical Review B 81 (2010) 081408.
URL `https://doi.org/10.1103/PhysRevB.81.081408`

[74] M. Dion, H. Rydberg, E. Schröder, D. C. Langreth, B. I. Lundqvist, Van der waals density functional for general geometries, Physical Review Letters 92 (2004) 246401.
URL `https://doi.org/10.1103/PhysRevLett.92.246401`

[75] R. Haumont, I. A. Kornev, S. Lisenkov, L. Bellaiche, J. Kreisel, B. Dkhil, Phase stability and structural temperature dependence in powdered multiferroic $BiFeO_3$, Physical Review B 78 (2008) 134108.
URL `https://link.aps.org/doi/10.1103/PhysRevB.78.134108`

[76] T. Ada, K. Nigussa, L. Deja, Impact of a dopant vis-a-vis site and concentration on the photovoltaic effect of $BiFeO_3$, Physica B: Condensed Matter 647 (2022) 414366.
URL `https://doi.org/10.1016/j.physb.2022.414366`

[77] N. Holzwarth, G. Matthews, R. Dunning, A. Tackett, Y. Zeng, Comparison of the projector augmented-wave, pseudopotential, and linearized augmented-plane-wave formalisms for density-functional calculations of solids, Physical Review B 55 (1997) 2005.
URL `https://doi.org/10.1103/PhysRevB.55.2005`

[78] R. Weast, CRC Handbook of Chemistry and Physics, CRCPress, Boca Raton, FL, 1997.

[79] F. D. Murnaghan, The compressibility of media under extreme pressures, Proceedings of the National Academy of Sciences 30 (1944) 244–247.
URL `https://doi.org/10.1073/pnas.30.9.244`

[80] M. Rajalakshmi, A. K. Arora, Stability of Monoclinic Selenium Nanoparticles, Solid State Physics 44 (2002) 109.

[81] S. Desgreniers, High-density phases of ZnO: Structural and compressive parameters, Physical Review B 58 (1998) 14102.
URL `https://doi.org/10.1103/PhysRevB.58.14102`

[82] Ü. Özgür, Y. I. Alivov, C. Liu, A. Teke, M. Reshchikov, S. Doğan, V. Avrutin, S.-J. Cho, Morkoç, H, A comprehensive review of ZnO materials and devices, Journal of applied physics 98 (2005) 11.
URL `https://doi.org/10.1063/1.1992666`

[83] P. Nozieres, D. Pines, Electron interaction in solids. Characteristic energy loss spectrum, Physical Review 113 (1959) 1254.
URL `https://doi.org/10.1103/PhysRev.113.1254`

[84] S. Suzuki, C. Bower, Y. Watanabe, O. Zhou, Work functions and valence band states of pristine and Cs-intercalated single-walled carbon nanotube bundles, Applied Physics Letters 76 (2000) 4007–4009.
URL `https://doi.org/10.1063/1.126849`

[85] K. Jacobi, G. Zwicker, A. Gutmann, Work function, electron affinity and band bending of zinc oxide surfaces, Surface Science 141 (1984) 109–125.
URL `https://doi.org/10.1016/0039-6028(84)90199-7`

[86] T. Jayasekera, S. Xu, K. W. Kim, M. B. Nardelli, Electronic properties of the graphene/6H-SiC $(000\bar{1})$ interface: A first-principles study, Physical Review B 84 (2011) 035442.
URL `https://doi.org/10.1103/PhysRevB.84.035442`

[87] X. Fan, W. Zheng, V. Chihaia, Z. Shen, J.-L. Kuo, Interaction between graphene and the surface of SiO_2, Journal of Physics: Condensed Matter 24 (2012) 305004.
URL https://dx.doi.org/10.1088/0953-8984/24/30/305004

[88] C. Gong, G. Lee, B. Shan, E. M. Vogel, R. M. Wallace, K. Cho, First-principles study of metal–graphene interfaces, Journal of Applied Physics 108 (2010) 123711.
URL https://doi.org/10.1063/1.3524232

[89] B. Das, B. Choudhury, A. Gomathi, A. K. Manna, S. Pati, C. Rao, Interaction of inorganic nanoparticles with graphene, ChemPhysChem 12 (2011) 937–943.
URL https://doi.org/10.1002/cphc.201001090

Declaration

I declare that the thesis hereby submitted to Addis Ababa University for the degree of Master of Science has not previously been submitted by me for a degree at this or any other university, that it is my own work both in design and execution, and that all material contained herein has been duly acknowledged.

Name: Hailu Diro

Signed: – – ––

Date: – – ––

e-mail: `hailudiro1993@gmail.com`

Place and time of submission

Addis Ababa University

Department of Physcs

March 23, 2023

This thesis has been submitted for examination with my approval as University adviser.

Name: Dr. Kenate Nemera

Signature: – – ––